THE UNIVERSITY OF CHICAGO

LOW-TEMPERATURE SCANNING TUNNELING MICROSCOPY AND SCANNING TUNNELING SPECTROSCOPY STUDY OF HYDROGEN AND NITROGEN DOPED NB(100) CRYSTALS

A DISSERTATION SUBMITTED TO

THE FACULTY OF THE DIVISION OF THE PHYSICAL SCIENCES

IN CANDIDACY FOR THE DEGREE OF

DOCTOR OF PHILOSOPHY

DEPARTMENT OF CHEMISTRY

BY

RICHARD DARREN VEIT

CHICAGO, ILLINOIS

DECEMBER 2019

Table of Contents

List of Figures

Acknowledgments

I would like to thank all of the people that helped make my Ph.D. possible. First, I would like to thank my advisor, Professor Steven Sibener, for accepting me into his group and making all of this work possible. I would also like to thank Professors Greg Engel and Sarah King for serving on my thesis committee.

I must thank my lab partners Dr. Rachael Farber and Sarah Willson. Without their help, my thesis would be much lighter than it is today. I owe my successes to them. I thank my lab neighbors, Dr. Jeff Sayler and Sarah Brown, for their companionship and enlightening scientific discussions throughout my time in graduate school. I also thank the rest of the Sibener Group for their knowledge, support, and assistance throughout my Ph.D.

Tanya Hagerman has been invaluable in assisting me in navigating the university purchasing system, and I thank her for ensuring that I had all of the equipment I needed to carry out all of my experiments. I give a huge thanks to Maria Jimenez for doing all that she does to keep the Sibener Group running smoothly.

I would like to thank Drs. Qiti Guo and Justin Jureller for their assistance with MRSEC equipment in the early years of my Ph.D.

I would like to thank Melinda Moore and Dr. Vera Dragisich for their assistance in departmental matters.

Finally, I would like to thank my parents, for their understanding and patience while I pursued this degree.

Abstract

Chemical and structural defects have a profound impact on the performance of niobium superconducting radio frequency cavities for particle accelerators. The properties of the first 40-100 nm of the cavity sub-surface determine the performance of the cavity because of the expulsion of the magnetic field in the superconducting state due to the Meissner effect. Chemical impurities present in this region that are introduced during standard fabrication techniques can severely hinder, or improve, cavity performance. Dissolved hydrogen in the cavity can precipitate out as niobium hydride phases on the cavity surface and cause local areas of reduced superconductivity or even quench if the hydrides are large enough. The interaction of hydrogen with other impurities affects the growth of hydride phases during cooldown. Many decades of R&D have now gone into developing surface treatments for the cavities to optimize performance.

This thesis focused on two projects that were each directly motivated by surface treatments for Nb SRF cavities that revolutionized cavity performance. Simply baking the cavities in a UHV furnace, or even in air, at very mild temperatures of 400-440 K eliminates the onset of the so called high Q drop-off on standard electropolished cavities. Given the mild temperature of this procedure, oxygen dissolution is likely to play a role. Nitrogen doping the cavities at the end of the UHV hydrogen degas has even more profound effects on cavity performance. Q is increased at all accelerating gradients, there is a reversal of the field dependence of Q in the medium field regime, and the high Q drop off is eliminated. The role of nitrogen in possibly suppressing the formation of nanoscale hydride features is the subject of intense interest and study in the SRF community.

The dissolution of the native niobium pentoxide layer was studied with Auger electron spectroscopy. An activation energy for oxygen dissolution from the surface into the bulk was calculated. The (3x1)-O ladder structures were characterized with scanning tunneling microscopy

before and after dissolution, and surface reconstructions of the ladders were observed after repeated oxygen dissolution. Nb(100) crystals were doped with hydrogen, nitrogen and hydrogen, and nitrogen only. Hydride growth and suppression were studied with scanning tunneling microscopy and scanning tunneling spectroscopy by cooling and holding the crystals at 100 K in the microscope stage through the use of a continuous flow liquid helium cryostat. Surface structural evolution and changes to the surface bandgap measured *via* STS were tracked over the course of many days while the crystal was kept cold. The surface bandgap was shown to significantly narrow relative to the blank ladders on the hydrogen doped surface. Additionally, the surface bandgap of the nitrogen as well as nitrogen and hydrogen infused sample widened relative to undoped Nb(100) at 100 K. These results provide the first structural and electronic characterization of initial Nb hydride growth and suppression behavior at the nano-scale.

Chapter 1: Introduction

1.1 Motivation: Niobium Superconducting Radio Frequency Accelerator Cavities

The key enabler of the modern particle accelerator is the superconducting radio frequency cavity, as it is the device which imparts energy to the charged particles.[1,2] The cavity is an electromagnetic resonator which imparts energy to the charged particles *via* the RF electric field at resonant frequencies typically between 50 and 4000 MHz depending on the application. The most important characteristics of these cavities for performance purposes are the quality factor, Q, and the average accelerating field, E_{acc}. The average accelerating field is typically reported in MV/m, and determines the total length of accelerator needed to accelerate the charged particles to their desired energy, depending on application. The quality factor is the ratio of the energy stored in the cavity to the energy lost in an RF period, and determines the power that is dissipated through the cavity walls during operation. Typically, one should strive for the highest E_{acc} and Q possible.

Historically, RF cavities were made from copper. A normal conducting cavity becomes an issue for applications requiring continuous wave (cw) operation, due to the high power dissipation of the normal conductor. This is where superconductivity comes to the rescue. The RF surface resistance of a superconductor is typically 5 orders of magnitude less than that of copper, meaning the Q is five orders of magnitude higher. To illustrate, at 500 MHz, a copper cavity must operate below 3 MV m^{-1} in cw to keep dissipation tolerable, while a superconducting cavity at 1300 MHz can operate at 16 MV m^{-1} at 2K.[2] Superconducting cavities are therefore the only way to economically provide the necessary voltage for high-energy applications.

Niobium is the superconducting material of choice for SRF cavities. This is for a number of reasons: it has the highest elemental superconducting critical temperature of 9.25 K leading to ultra-low RF surface resistance at 2 K, the material is readily available, and it has a high degree of

malleability which is necessary for molding the cavities into the complex geometries required for operation. The metallurgy of Nb had also already been thoroughly studied in the literature because of its applications in other industries, such as the manufacture of stainless steel alloys and superalloys for aerospace applications.

Niobium cavities undergo extensive surface processing following fabrication from high-purity Nb sheets.[3] The surface processing includes polishing procedures such as centrifugal barrel polishing, electropolishing, and buffered chemical polishing. These steps are necessary for removing defects introduced during the fabrication process. A major issue during surface polishing is the absorption of hydrogen into the bulk niobium from the ambient. Absorbed hydrogen is known to precipitate out as lossy niobium hydrides during cooldown and cause significant RF losses.[4-7] Niobium hydrides are weakly superconducting at 2 K and are known to cause local areas of reduced superconductivity and therefore increased surface resistance on cavity surfaces. Large hydrides cause superconductivity quench because of proximity effect breakdown and are responsible for what is called "hydrogen *Q* disease", which is characterized by orders of magnitude reduced *Q* at the onset of RF power which renders the diseased cavities inoperable. Degassing the cavities at 1100 K in a vacuum furnace after polishing eliminates the *Q*-disease, but hydrogen contamination in the Nb and smaller hydrides still persist after cooldown. After heat treatments, the cavities undergo high-pressure rinsing with ultrapure water to eliminate any chemical and particulate residue from the interior surface, and finally transferred to a dust-free clean room with plumbing still attached for draining and final assembly.

The surface resistance in the superconducting state is determined by the material properties of the first 40-100 nm of the cavity wall due to the Meissner Effect. Chemical and structural defects in this region can have a profound impact on cavity performance, and depending on the defect, can

either improve or degrade cavity performance. This is clearly illustrated by the formation of niobium hydrides during cooldown, which can decrease Q by orders of magnitude, and by the nitrogen doping of the cavities, which produces reliable increases to Q and a reversal of the field dependence in the medium field regime, which will be discussed shortly. Understanding the interactions between these impurities and the surrounding Nb lattice is essential to understanding the mechanisms which to lead to the improvement and degradation of the Q of the cavities. Our scanning tunneling microscopy and scanning tunneling spectroscopy measurements that are presented in this thesis add to the mounting experimental evidence to provide explanations behind revolutionary cavity surface treatments that are being employed around the world in the fabrication of state-of-the-art accelerator facilities. The direct motivation for the experiments outlined in this thesis come from two separate discoveries that revolutionized SRF cavity surface preparation procedures at the time of their inception. They are discussed in further detail in the following sections.

1.2 Mild Baking and Nitrogen Doping of Niobium SRF Cavities

The mild baking of Nb SRF cavities in vacuum or even in air has profound effects on Q_0 and particularly the onset of the high-field Q_0 drop.[8-10] This discovery was the principle motivation behind my initial research project presented in this thesis (Chapter 3), on oxygen dissolution and surface oxide reconstructions on Nb(100). First discovered in the early 2000's, heating the cavities in vacuum, or even in air, at temperatures of just 390-430 K for times of 24-48 hours produced profound effects on the onset of the high-field Q_0-drop. At these mild temperatures oxygen diffuses much more rapidly than other common impurities such as nitrogen and carbon, and studies suggest oxygen dissolution and interstitial oxygen could play a role in the mild bake improvements to the

Q.[10] It should be noted that the mechanism behind the mild bake is not fully understood and is still a topic of debate in the SRF community.

It is well know that niobium is covered in an ever-present dielectric oxide layer that is ~5 nm thick. The outermost region of the oxide layer, at the gas-surface interface, is Nb_2O_5, on top of a homologous series of sub-oxides (NbO_x with $x \sim 0.5 - 2$) before the bulk metal is reached. Previous photoemission studies had demonstrated that at these temperatures both the composition and thickness of the native niobium pentoxide layer changes as the pentoxide is reduced and freed oxygen is promoted to diffuse from the surface into the bulk metal.[11-14] The mild bake effect is stable after re-oxidation by exposure to air, so it was clear that it was not the presence of the oxide layer that was responsible for the improved *Q*, but it was strongly suspected that oxygen dissolution played at least significant role in the observed improvements.

I was awarded a Fermilab Fellowship at the onset of my second year at the University of Chicago to study SRF relevant processes. During my early discussions with scientists at Fermilab, it was clear that it was still not entirely understood when the oxide layer was present and to what extent during various thermal treatments to the cavity samples. This was the motivation for my initial experiments, which involved monitoring the oxygen content on the Nb(100) surface with Auger electron spectroscopy (AES) while heating the crystal at various temperatures of interest. Nb(100) is the model system that I used for all experiments outlined in this thesis and will be discussed in detail in a later section. I then took scanning tunneling microscopy measurements of the Nb(100) (3x1)-O ladder structures (to be discussed later) before and after oxygen dissolution in order to provide the first atomic-scale visualization of, if any, the structural changes to the oxide/metal interface that resulted from oxygen dissolution.

After my initial experiments, it was clear that the hot button topic in the SRF community at the time was the nitrogen doping of the cavities, which had just been recently discovered.[15] Discovered by accident, the scientists at Fermilab had added a nitrogen exposure step to the end of the 1100 K anneal in UHV. The initial goal had been to create a NbN layer at the surface, due to the higher critical of temperature of NbN over pure Nb. When the cavities were *Q*-tested afterwards, the *Q* was degraded by orders of magnitude relative to a standard EP degassed cavity. In order to reproduce the original Nb surface, the cavities underwent further electropolishing to remove the layer created by the doping. It was quickly observed that the *Q* was consistently higher on cavities that had undergone nitrogen doping and further surface material removal than on the standard EP, degassed cavities. After a number of experiment replications, it was concluded that the nitrogen doping was reliably increasing the *Q* at all operating gradients and reversing the field dependence in the medium field regime, which was truly remarkable. The initial theory was that interstitial nitrogen that had diffused into the cavity sub-surface during the doping process was responsible for the observed benefits. It was believed that the nitrogen was serving as a hydrogen "trap", preventing these smaller, nanoscale hydrides from precipitating during cooldown. Studying the formation of hydrides on the atomic and nanoscale and the subsequent effects of nitrogen doping served as the motivation for the remainder of my thesis work.

1.3 Model System Nb(100) (3x1)-O Oxide Ladder Structures

The system used for these experiments was the Nb(100) (3x1)-O ladder structures. This surface was first characterized with STM and published in 2001,[16] and then again in 2003,[17] after they were more fully understood. We chose this surface because it provides a well-characterized, atomically-flat surface for STM studies. Niobium SRF cavities are made from bulk niobium, so

the cavity surfaces are polycrystalline, and the roughness of the polycrystalline surface makes it experimentally prohibitive to study atomic scale processes with the STM. The (3x1)-O surface is produced by repeated cycles of argon ion sputtering and annealing at 2100 K in UHV. Single crystals arrive with a plethora of contaminants and impurities from the lab at which they were grown and cut and require extensive cleaning in UHV in order to produce clean surfaces for STM experiments. Annealing brings impurities from the bulk to the surface and then ion sputtering is used to remove them. Niobium binds oxygen very strongly, and an oxygen free niobium surface is only achieved after extensive sputtering and annealing at 2500 K. My experimental goals never required an oxygen free surface, so I never spent the time to try and accomplish this. The ladder structures are the result of the epitaxial growth of NbO on Nb.[17] From Auger electron spectroscopy measurements, after the ladders are produced, the ratio of oxygen to Nb within the Auger electron escape depth is about 22% at an Nb surface temperature of 300 K. The surface was cleaned until all that remained by AES was Nb and oxygen in this ratio. This process took about a month.

A typical STM image of the (3x1)-O ladders is shown in **Figure 1.1**. The ladders appear as a bright serpentine like structure on the surface. The bright protrusions, or rungs of the ladder structures, are parallel pairs of surface layer Nb atoms on the NbO(100) face. The dark depressions are oxygen. The distance between the rungs is a constant and is approximately 1.0 nm, or 3 times the Nb lattice parameter in the (100) plane. The width of the rungs is not a constant but rather distributed in a range, as is discussed in detail in Chapter 3 of this thesis. On the unperturbed ladders, the distribution is centered on a width of 10 Nb atoms, or 3.3 nm. First principles calculations have found that the width of the ladder structures is governed by the NbO/Nb lattice mismatch, and that NbO is two layers thick.[18] Two orthogonal domains are observed. The monatomic step height is 0.17 nm.

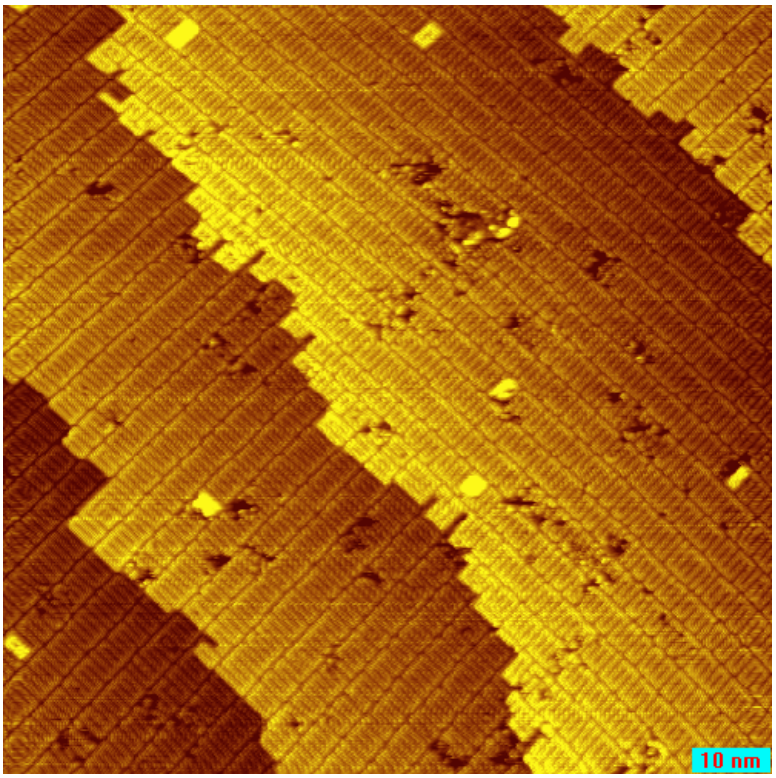

Figure 1.1 Typical STM image of the Nb(100) (3x1)-O ladder structures. This surface structure was produced by repeated Argon ion-sputtering and annealing the Nb(100) crystal at 2100 K in UHV. Imaging conditions: T_c = 300 K. Imaging conditions: 0.75 V, 131 pA.

1.4 References

1. Padamsee, H.; Knobloch, J.; Hays, T. *RF Superconductivity for Accelerators*; John Wiley & Sons: New York, 1998; chapter 1.
2. Padamsee, H.. 50 years of success for SRF accelerators – a review. *Supercond. Sci. Technol.* **2017,** *30,* 053003.
3. Padamsee, H.; Knobloch, J.; Hays, T. *RF Superconductivity for Accelerators*, John Wiley & Sons: New York, 1998; chapter 6.
4. Padamsee, H.; Knobloch, J.; Hays, T. *RF Superconductivity for Accelerators*, John Wiley & Sons: New York, 1998; chapter 9.
5. Barkov, F.; Romanenko, A.; Trenikhina, Y.; Grassellino, A. Precipitation of hydrides in high purity niobium after different treatments. *J. Appl. Phys.* **2013,** *114,* 164904.
6. Romanenko, A.; Barkov, F.; Cooley, L. D.; Grassellino, A. Proximity breakdown of hydrides in superconducting niobium cavities. *Supercond. Sci. Technol.* **2013,** *26,* 035003.
7. Barkov, F.; Romanenko, A.; Grassellino, A. Direct observation of hydrides formation in cavity-grade niobium. *Phys. Rev. Spec. Top. - Accel. Beams.* **2012,** *15,* 122001.
8. Ciovati, G. Review of the frontier workshop and *Q*-slope results. *Physica C*. **2006,** *441,* 44-50.
9. Ciovati, G.; Kniesel, P.; Myneni, G. Effect of Low Temperature Baking on Niobium Cavities. *Proceedings of the 11th Workshop on RF Superconductivity*. Lübeck/Travemünder, Germany, 2003.
10. Ciovati, G. Review of high field Q slope, cavity measurements. *Proceedings of the 13th Workshop on RF Superconductivity*. Beijing, China, 2007.
11. Hu, X.P.; Li, Y.P.; Ji, M.R.; Hu, J.X. The Interaction of Oxygen with Niobium Studied by XPS and UPS. *Solid State Commun.* **1989,** *71,* 849.

12. Sanz, J.M.; Hoffman, S. Auger Electron Spectroscopy and X-Ray Photoelectron Spectroscopy Studies of the Oxidation of Polycrystalline Tantalum and Niobium at Room Temperature and Low Oxygen Pressures. *Journal of the Less-Common Metals*. **1983,** *92,* 317-327.
13. Lindau, I.; Spicer, W.E. Oxidation of Nb as Studied by UV-Photoemission Technique. *J. Appl. Phys.* **1974,** *45,* 3720.
14. Oechsner, H.; Giber, J.; Füber, H.J.; Darlinski, A.. *Thin Solid Films*, **1985**, *124*, 199.
15. Grassellino, A.; Romanenko, A.; Sergatskov, D.; Melnychuk, O.; Trenikhina, Y.; Crawford, A.; Rowe, A.; Wong, M.; Khabiboulline, T.; Barkov, F. Nitrogen and argon doping of niobium for superconducting radio frequency cavities: A pathway to highly efficient accelerating structures. *Superconducting Science Technology*. **2013,** *26,* 102001.
16. Li, Y.; An, B.; Xu, X.; Fukuyama, S.; Yokogawa, K.; Yoshimura, M. "Surface structure of niobium- dioxide overlayer on Nb(100) identified by scanning tunneling microscopy," *Journal of Applied Physics.* **2001,** *89,* 4772–4776.
17. An, B.; Fukuyama, S.; Yokogawa, K.; Yoshimura, M. .Surface structures of clean and oxidized Nb(100) by LEED, AES, and STM. *Physical Review B.* **2003,** *68,* 115423.
18. Wen, M.; An, B.; Fukuyama, S.; Yokogawa, K. First-Principles Study of Oxidized of Nb(100) Surface Structures. *Surface Science*. **2009,** *603,* 216-220.

Chapter 2: Experimental

2.1 UHV Facilities and Instrumentation

All experimental results presented in this thesis were obtained on an ultra-high vacuum variable temperature scanning tunneling microscope (UHV VT-STM). The instrument is shown in **Figure 2.1**. The instrument comprises three differentially pumped UHV chambers, each of which are isolated from each other with gate valves. These chambers include two experimental chambers, an STM chamber and a sample preparatory chamber, and a load lock. All three chambers can be pumped down from air through the load lock with a turbomolecular pump backed by an oil-free roughing scroll pump. The turbo pump can get the chambers down to ~1.0×10^{-8} torr. The two experimental chambers are then each equipped and pumped on continuously with 200 L Gamma Vacuum Titan Ion Pumps. The ion pumps are each equipped with titanium sublimation pumps (TSPs). The TSPs are necessary for pumping out residual hydrogen. To reach UHV levels, the entire instrument is baked at 385 K for 48 hours after any time an experimental chamber has to be vented to air. The base pressure after bakeout of the STM chamber is $\leq 5.0\times10^{-11}$ torr, and the base pressure of the prep chamber is $\leq 1.0\times10^{-10}$ torr. STM tips and samples are loaded into the instrument *via* the load lock and pumped down to vacuum for transfer to the experimental chambers with a magnetic transfer arm.

The microscope chamber contains an RHK Beetle VT-STM. Images of the microscope stage and scan head both retracted and lowered onto the sample puck for approach are shown in **Figure 2.2a** and **2.2b**. The RHK six-contact sample puck outside of vacuum is also shown in **Figure 2.2c**. The Beetle scan head is equipped with a piezoelectric scan tube that holds the conducting tip and three piezoelectric legs which are used along with the scan tube to control approach and the position of the tip during imaging. Control voltages are delivered to the piezos *via* the angle hair copper wires

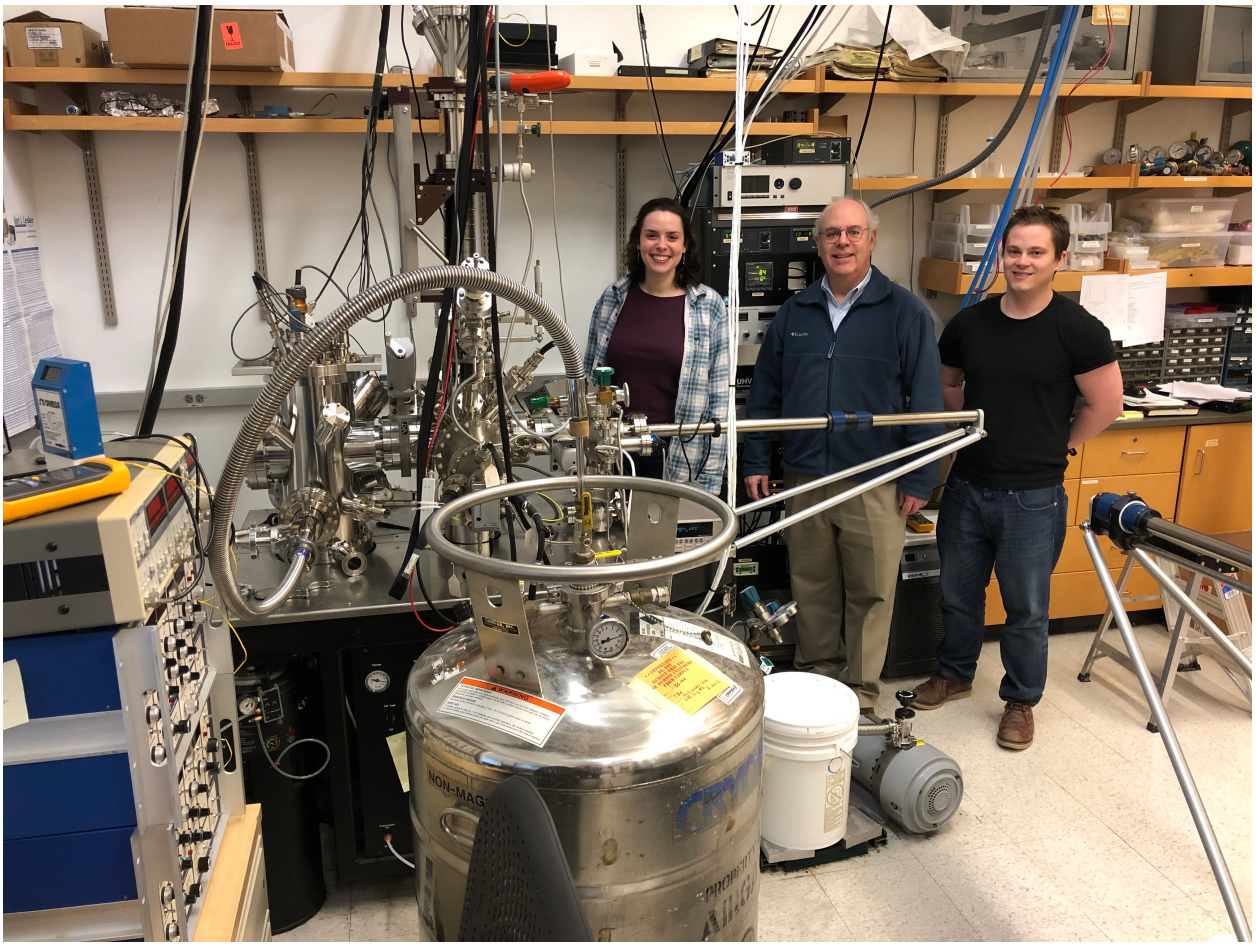

Figure 2.1 UHV VT-STM facilities for SRF measurements in the Sibener Group (liquid helium dewar shown attached to microscope chamber *via* continuous flow cryostat for cryogenic measurements). Pictured from left to right behind the instrument in the picture are Dr. Rachael Farber, Prof. Steven Sibener, and myself, Darren Veit.

attached to the scan head. Coarse approach is accomplished by walking the scan head down the puck ramp with the three piezo legs. Fine approach is accomplished by extending the scan tube to "feel" for tunneling current. If none is detected, the legs take a single step further down the ramp, and this process is repeated until tunneling current is detected. STM data can then be collected attemperatures from ~25 K to 373 K. A liquid helium dewar is shown attached to the STM stage in **Figure 2.1** for cryogenic measurements. dIdV is measured with an external lock-in amplifier (Stanford Research Systems, SR830 DSP).

The preparatory chamber is equipped with Auger electron spectroscopy (AES), x-ray photoelectron spectroscopy (XPS), an ion sputter gun, and a residual gas analyzer (RGA). The prep chamber staged is equipped with filament connections for electron beam heating and is cooled with a liquid nitrogen coldfinger. The crystal was cleaned in the prep chamber *via* cycles of Ar^+ ion sputtering and annealing at 2100 K. The temperature was measured using an infrared pyrometer (Mikron Infrared, MG-140) mounted outside of the UHV chamber. Heating was accomplished *via* electron-beam heating, using a hand-coiled thorium doped tungsten filament placed in very close proximity to the bottom of the crystal in the sample puck. The shelf of the RHK six-contact puck was mechanically removed for the electron beam heating. Because of the absence of the shelf, 0.8 mm tantalum wires were spot welded to the back of the crystal and held in the RHK stage clips during imaging for stability. For the heating, the filament was biased at -600 V relative to the crystal (emission 100 mA). I feel it important enough to note that the proximity to the crystal of the filament is very important for e-beam heating, because any residual gas between the filament and the crystal will inelastically scatter the electrons. Producing and mounting a good, reliable filament required repeated efforts early in the process. Surface cleanliness was confirmed with AES, XPS, and STM analysis.

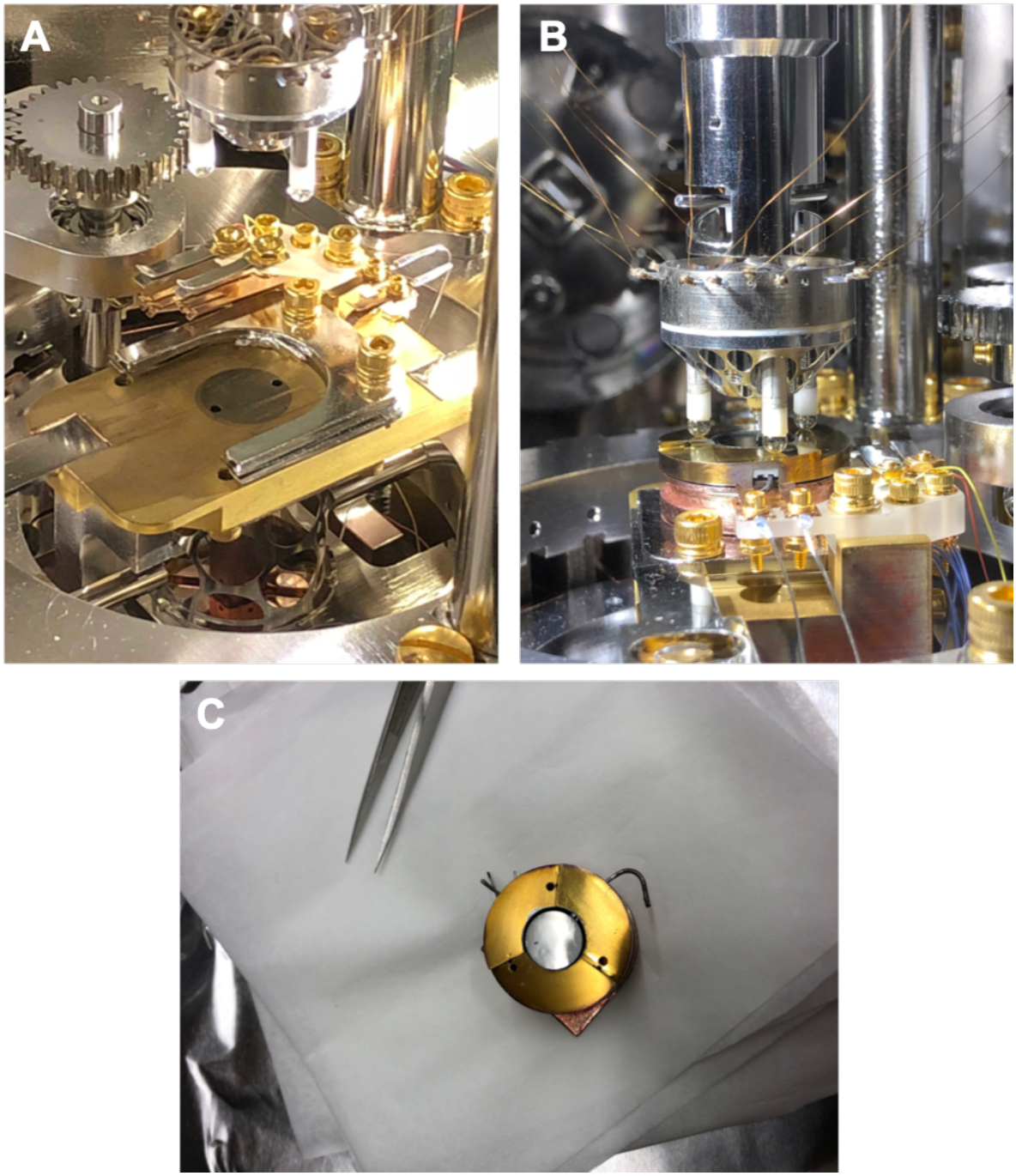

Figure 2.2 Images of the STM stage with **A:** scan head fully retracted; **B:** STM stage with scan head lowered onto sample puck; **C:** and sample puck out of vacuum.

2.2 Scanning Tunneling Microscopy and Scanning Tunneling Spectroscopy

The primary techniques employed for all of the experiments presented in this thesis were scanning tunneling microscopy (STM) and scanning tunneling spectroscopy (STS). Invented in 1981,[1] and whose inventors were awarded the Nobel Prize in Physics for its invention in 1986, STM is now a widely known and employed technique for atomic and nanoscale visualization of conducting surfaces. **Figure 2.3** provides a schematic on the basic concepts involved in the operation of the machine.

A conducting tip is brought within a few angstroms of a conducting surface with an applied bias between them and current tunnels across the vacuum gap either from tip to surface or surface to tip depending on the applied bias. This tunneling signal is sent to a current preamplifier which converts it to a voltage and sends the signal to the control electronics. A feedback loop processes any difference between the signal and current setpoint and sends corrective voltages to the piezo scan tube to maintain the tunneling setpoint.

As mentioned, the positioning of the STM tip is controlled with a piezoelectric scan tube. Piezoelectric materials exhibit a permanent dipole which means a voltage is produced when mechanical force is applied. The reverse is true as well; when a voltage is applied, the piezo will bend. By applying voltages to the scan tube, the positioning of the tip can be controlled with great precision. In this microscope, the piezo motion in the x and y directions is 20 nm per applied volt. The maximum applied voltage is ±130 V in each direction, giving a lateral range of motion of about 2.5 microns in the x and y while the STM is in tunneling range. The lateral resolution of the microscope is then limited by the curvature of the tip and can get down to about 1 angstrom.

The vertical resolution of the microscope is governed by the tunneling current. Electron tunneling is a quantum mechanical phenomenon where an electron's wave function remains

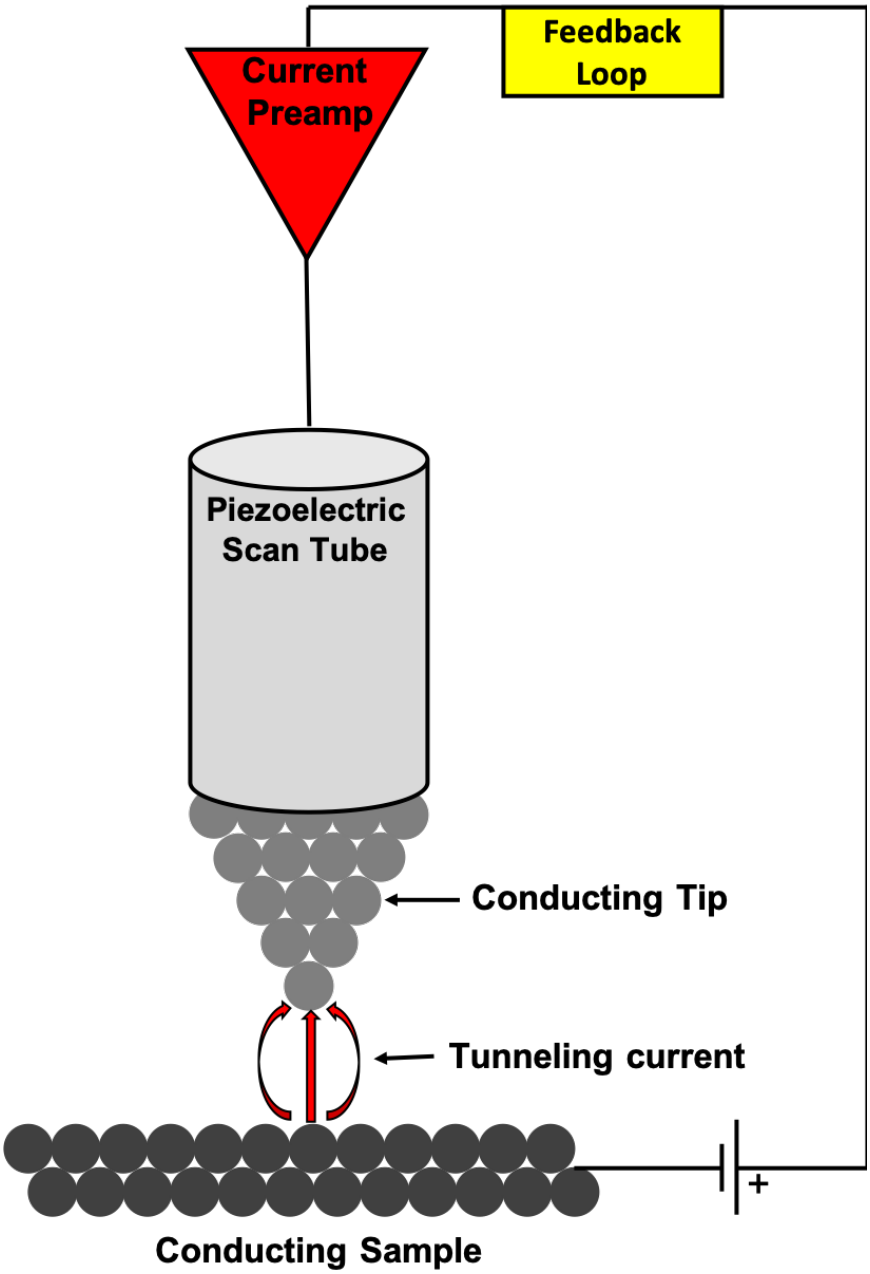

Figure 2.3 Simplified schematic of STM operation. An applied bias to the conducting sample relative to the conducting tip causes electrons to flow across the vacuum gap between them. The tunneling signal is sent to a current preamplifier which converts it to a voltage and sends it along to the control electronics which then sends correcting voltages to the STM piezos to maintain the tunneling current setpoint.

non-zero in classically forbidden potential barriers, allowing electrons to flow, or tunnel, through the barrier. Mathematically, the rate of tunneling can be found using the Wentzel-Kramers-Brillouin (WKB) approximation. This approximation assumes that when an electronic potential is slowly varying, the amplitude of the wave function within the potential will also slowly vary. This gives the expression for the tunneling current :

$$I = \int_0^{eV} \rho_s(E)\rho_t(eV - E)T(E, eV)dE \tag{2.1}$$

where ρ_s is the density of states of the sample, ρ_t is the density of states of the tip.[2] The transmission function T(E,eV) is as follows:

$$T(E, eV) = \exp\left(-\frac{-2Z\sqrt{2m}}{\hbar}\sqrt{\frac{\phi_s+\phi_t}{2} + \frac{eV}{2} - E}\right) \tag{2.2}$$

where ϕ_s and ϕ_t are the work functions of the sample and tip and Z is the distance of the tip from the sample surface.[2]

The transmission probability function is exponentially dependent on the length of the vacuum gap, as well as the barrier height. The exponential decay of the tunneling current with distance from the surface provides the vertical resolution of the STM, which is about 0.1 angstroms.

The STM operates by rastering across the surface, probing the local electronic density of states. When the local density of states of the surface is constant, the contrast in the image comes entirely from topography. When the LDOS of the surface is not constant, the image is a convolution of LDOS and topography. It is typical during STM imaging to image with a wide range of applied biases to observe any bias dependence in the imaging. Topographical features will not change depending on bias, while contrast coming from changing LDOS will change when the bias is changed.

This dependence of tunneling current on LDOS can be a nuisance for imaging, but provides an experimental method of probing electronic structure. In scanning tunneling spectroscopy (STS), the feedback loop is disabled, the height of the tip above the surface is held constant, and the applied bias is ramped to produce an I(V) curve. An external lock-in amplifier directly measures *dIdV* instead of having to numerically differentiate the obtained IV curve to minimize noise. The derivative of equation 2.1 with respective to voltage is strongly dependent of the electronic density of states, which can be seen as follows:

$$\frac{dI}{dV} = \rho_s(r, eV)\rho_t(r, 0)T(eV, eV, r) + \int_0^{eV} \rho_s(r, E)\rho_t(r, e - eV)\frac{dT(E, eV, r)}{dV}\, dE \qquad (2.3)$$

At a fixed location the transmission function increases smoothly and monotonically with tip-sample bias in the WKB approximation, so the structure in *dI/dV* can be assigned to features in the density of states in the first term of the equation.[3]

dI/dV was used extensively in the experiments outlined in this thesis to measure the surface bandgap on the model system Nb(100) (3x1)-O ladder structures. The purpose of this was to determine if we could differentiate between the clean oxide, hydrogen doped, and nitrogen doped ladder structures.

2.3 Auger Electron Spectroscopy and X-ray Photoelectron Spectroscopy

Auger electron spectroscopy (AES) and x-ray photoelectron spectroscopy (XPS) are both widely known and used analytical techniques for surface chemical analysis. XPS relies on the photoelectric effect, first described by Einstein in 1905, while AES relies on the Auger effect, first described not long after in the 1920's.[4] The photoelectric effect is simply the emission of electrons from a material when irradiated with photons of a sufficient energy, while the Auger effect involves the ejection of outer shell electrons following a series of electronic relaxation events

following the emission of a core electron from an excited atom. In XPS X-ray radiation is used to excite surface atoms, while AES employs a focused incident electron beam. Both techniques measure the kinetic energy of the ejected electrons with an electron energy analyzer. For all of the experiments described in this thesis, a STAIB DESA 100 cylindrical mirror analyzer (CMA) was used to for the spectroscopic analysis. The energy resolution of this analyzer can be tuned from 70 meV to 6 eV. Both techniques are surface sensitive, sampling just the top few nanometers of the surface at most, because the escape depth of the ejected electrons is shallow due to a short inelastic mean free path. Both techniques must be performed under UHV conditions, because residual gas between the surface and analyzer can interfere with the measurement.

In AES, surface atoms are first excited with a focused incident electron beam (3.00 keV, 20 nA target current). A core level electron is ejected from an excited atom, and an outer shell electron drops down to fill the vacancy created by the ejected electron. This energetically favorable process releases energy which can then go on to eject another outer shell electron. This second ejected electron is an Auger electron. The kinetic energy of an Auger electron is an intrinsic property of the parent atom, so the kinetic energies can be used to identify and quantify the chemical species present within the AES sampling depth. Larger elements produce many unique Auger electrons, and each electron can be distinguished by the electronic transition that produced it.

The X-ray source used in our instrument is a SPECS XR50 dual-anode source. The source contains both an aluminum and magnesium anode, and produces Al kα (1486.6 eV, 0.85 eV line width), and Mg kα (1253.6 eV, 0.7 eV line width) X-rays to irradiate the sample surface. The X-rays excite the surface atoms which eject core-level photoelectrons which can then be analyzed by their kinetic energy to identify and quantify the chemical properties of the surface. The kinetic

energy of the ejected photoelectron is dependent on the energy of the incident X-rays, the electron binding energy, and the work function of the detector, so the binding energy can be easily determined by the equation:

$$E_{binding} = E_{photon} - (E_{kinetic} + \phi)$$

where the kinetic energy is measured, the energy of the X-rays is known, and the work function (ϕ) is dependent on both the detector and the material, and is a simple instrumental correction factor that can be tuned with known reference samples. The binding energy of an electron is dependent on its chemical environment, so XPS is a very useful tool for determining both the elements present on your surface and their oxidation state.

2.4 References

1. Binnig, G.; Rohrer, H.; Gerber, Ch.; Weibel, E. Surface Studies by Scanning Tunneling Microscopy. *Physical Review Letters*. **1982,** *49,* 57-61.
2. Hamers, R.J. Methods of Tunneling Spectroscopy with the STM. In D. Bonnell (Ed.), *Scanning Probe Microscopy and Spectroscopy: Theory, Techniques, and Applications, 2nd Edition*. Weiley-VCH: New York, 2001.
3. Wiesendanger, R. *Scanning Probe Microscopy and Spectroscopy: Methods and Applications*. Cambridge University Press: New York, 1994.
4. Briggs, D.; Grant, J.T. *Surface Analysis by Auger and X-ray Photoelectron Spectroscopy*. IM: Chichester, 2003.

Chapter 3: Oxygen Dissolution and Surface Oxide Reconstructions on Nb(100)

The ever-present native oxide layer on niobium plays a fundamental role in the performance of Nb superconducting radio frequency (SRF) cavities for particle accelerators and light sources. Using Nb(111) and Nb(100) as model systems, oxygen dissolution and surface structural evolution as a function of thermal treatments in ultrahigh vacuum (UHV) were studied using combined Auger electron spectroscopy (AES) and scanning tunneling microscopy (STM), providing novel, real space information regarding the complex evolution of the Nb surface oxide. The surface crystallographic orientation was shown to influence oxide surface structure; Nb(111) displayed disordered surface oxide domains while Nb(100) was comprised of well-ordered, (n×1)-O domains. The temperature-dependent dissolution of the native oxide layer on Nb(100) was characterized to ascertain the energetics for oxygen dissolution, and evolution of the surface oxide superlattice structure following thermal annealing was observed with STM. By understanding the kinetic behavior of oxygen dissolution during thermal annealing and subsequent structural evolution of the Nb(n×1)-O superlattice on Nb(100), a more thorough understanding of the complex interactions driving chemical composition and cavity surface structure under Nb SRF cavity processing and operating conditions may be understood.

3.1 Introduction

Niobium (Nb) is the current material of choice for superconducting radio frequency (SRF) cavities for particle accelerators due to its ultralow surface resistance (Rs) and high cavity quality factor (Q) at operating temperatures ≤ 2 K.[1-4] To ensure optimal SRF cavity performance, much work has been done to characterize factors impacting SRF cavity performance and to improve

cavity preparation techniques.[5-9] It was determined through these studies that Nb superconductivity is dependent on the chemical and structural properties of the first 40–100 nm of the interior cavity surface.[1] Under actual Nb SRF cavity fabrication and operating conditions, an ever-present native oxide layer covers the entirety of the Nb surface, and the surface structure and chemical identity of the oxide layer directly effects SRF cavity performance. During electrochemical polishing procedures that remove ≈ 120 μm of the cavity surface, the Nb oxide layer is stripped, allowing the rapid incorporation of hydrogen into the Nb cavity;[7,10,11] immediately following electrochemical polishing, the native oxide reforms, effectively trapping the absorbed hydrogen. This incorporated hydrogen segregates to the surface of Nb cavities forming Nb hydride features that quench superconducting behavior, and significant work is being done to identify beneficial dopants to inhibit the growth of harmful Nb hydride species.[2,12,13] In addition to the formation and removal of the native oxide allowing the incorporation of harmful or beneficial chemical dopants, the quality of the native oxide directly effects the formation of uniform thin films of high efficiency alloys, such as Nb_3Sn.[14] Nb_3Sn has a lower Rs than Nb as a function of temperature, resulting in higher Q factors at a given temperature, thus improving the performance of particle accelerator facilities.[15-17] Results suggesting the importance of the native oxide characteristics and quality influencing Nb_3Sn growth further supports the continued interest in understanding the behavior of Nb oxide under fabrication and operating conditions. It is, therefore, imperative to obtain a fundamental understanding of the complex interplay between surface and near surface chemical species and evolution of the native Nb oxide surface structure under various fabrication and operating conditions.

Particular emphasis on elucidating the intermolecular interactions between Nb and impurities such as oxygen, hydrogen, nitrogen, and carbon which significantly influence SRF

cavity Rs and Q is especially relevant.[2-5,7,8,10-13] Nb readily binds oxygen, and the oxidation of Nb and subsequent effect on superconductivity is of great interest and has been extensively studied in the past.[18-34] It was determined that bulk oxide films quench superconductivity while thin films of surface oxide do not effect superconducting behavior to such a large degree. In operational SRF cavities, mild baking of the cavities at 400 – 500 K in vacuum or air has profound effects on cavity performance,[1,7,9] and it is necessary to understand the complex surface evolution that occurs during the initial stages of oxidation. The initial stages of Nb oxidation have been investigated using a variety of ultrahigh vacuum (UHV) surface science techniques such as Auger electron spectroscopy,[20-24,35,36] x-ray photoelectron spectroscopy (XPS),[23,24,30,37] ultra-violet photoelectron spectroscopy (UPS),[23,25,26] electron energy loss spectroscopy (EELS),[18,22,26] mirror electron microscopy,[35] and secondary ion mass spectrometry (SIMS).[21,22] Such studies have revealed complex interactions between oxygen and Nb, and that producing a clean, oxygen-free Nb surface is experimentally extremely difficult.[18-23,26,36] This is due to the high reactivity of Nb to oxygen and a strong preference for oxygen surface segregation. Farrell et al.[20] found that oxygen was detected on the Nb surface using AES at temperatures up to 1900 K, and Nb samples on the order of 1300 K with bulk oxygen concentrations well below the bulk solubility limit still exhibited roughly quarter monolayer surface oxygen coverage. Oxygen removal occurs via desorption of oxygen incorporated into NbO and NbO_2 and begins at temperatures greater than 1900 K in UHV;[18,35,38] complete oxygen removal is only achieved at temperatures greater than 2500 K.[18,20,21,35,36]

Due to the high reactivity of Nb to oxygen, exposure of a cleaned Nb surface to low pressures of oxygen at room temperature results in oxygen chemisorption[18,21,22] and the subsequent formation of NbO, NbO_2, and Nb_2O_5 oxidic phases.[18,21-23,25,26] The surface oxide layers at

atmospheric pressure are comprised of Nb_2O_5, NbO_2, NbO, as well as metal-rich suboxides.[39] The Nb_2O_5 bulk pentoxide is most stable under ambient conditions and is the dominant oxide phase on the surface when present.[39] Removal of Nb_2O_5 is achieved when the sample is annealed in UHV above 600 K; Nb_2O_5 is reduced to NbO_2 and then NbO as oxygen is dissolved in the bulk of the metal.[30,37,40] The morphology of the niobium surface during thermal cleaning and oxidation has been studied in the past with low energy electron diffraction (LEED).[20,29,35,36]

More recently, atomically resolved structures have been observed on Nb(100)[33,34,41-43] and Nb(110)[31,32,44] with scanning tunneling microscopy (STM). On Nb(110), a surface comprised of quasiperiodical features is reported after Ar+ ion sputtering and annealing between 1200–2200 K in UHV.[31.32.44] An et al. provide a thorough review of the oxygen-induced structures that form on Nb(100).[41] As a result of thermal cleaning in UHV, a (3×1)-O structure forms as a result of the epitaxial growth of NbO/Nb above 873 K. A less oxygen-rich (4×1)-O structure forms after annealing the (3×1)-O structure at 2270 K as a result of oxygen desorption at higher annealing temperatures. While the two ladder structures, (3×1)-O and (4×1)- O, have been well characterized, no studies have been done investigating the energetics of oxygen dissolution at elevated temperatures relevant to Nb SRF cavity fabrication, nor has the surface evolution of the oxidized surface following thermal annealing been elucidated. To better understand the mechanism for oxygen dissolution of (3×1)-O/Nb(100), our study focuses on the atomic-scale structural evolution and kinetics of the (3×1)-O structure as a result of oxygen dissolution of the surface oxide layers on Nb(100).

3.2 Experimental

Experimental Niobium single crystals oriented to the (111), (110), and (100) faces with 99.99% purity were obtained from Surface Preparation Laboratory. The crystals were mounted in

a custom RHK six-contact sample puck with the interior shelf mechanically removed to hold a hand-coiled thoriated tungsten filament for electron-beam heating. The crystals were put into a custom UHV preparatory chamber equipped with AES, XPS, ion sputtering, and a Residual Gas Analyzer (RGA). The chamber has a base pressure of $\leq 1.0\times10^{-10}$ torr. The crystal surfaces were cleaned by cycling between Ar+ ion sputtering for 30 min and annealing at 2100 K for 10 min. The surface temperature was monitored with an infrared pyrometer mounted outside of the UHV chamber. All scanning tunneling microscopy (STM) images were taken at room temperature using an RHK Variable Temperature Beetle-style STM kept in an adjoining UHV chamber with a base pressure of 5.0×10^{-11} torr. Mechanically cut Pt/Ir (0.8Pt/0.2Ir) was used for the STM tip and no additional conditioning or sharpening of the tip was performed. STM measurements were performed in constant-current mode. No appreciable bias dependence was observed in the STM images. For the AES kinetic measurements, native oxide layer was grown by exposure to atmosphere following the aforementioned cleaning methods in UHV. To study structural evolution of the oxidized Nb(100) surface, in situ oxygen exposure was performed while the crystal was in the STM stage by introducing ultra-high purity oxygen gas to the UHV chamber through a variable leak valve. The crystal was held at room temperature during exposure, and the STM tip was retracted out of tunneling range.

3.3 Results and Discussion

STM images of Nb(100) and Nb(111) after preparation are shown in **Figure 3.1**. Despite heating the Nb(111) surface for more than 3 hours at 2100 K, and with a clean AES spectra, only disordered clusters were observed in the STM images (**Figure 3.1A**). While these clusters do have some internal structure, there is no obvious long-range order present on the surface. The Nb(100)

crystal, however, was prepared in the same manner and regular (3×1)-O ladders covered the crystal surface. As the only difference between the two crystals is the orientation of the surface atoms, the surface geometry of the Nb crystal must play a significant role in the ordering of NbO. We note that niobium is a classic bcc crystal with a bulk lattice parameter of 330.04 pm. The (111) plane, therefore, has an interatomic distance of 466.7 pm, while the spacing in the (100) plane is equal to the bulk lattice parameter of 330.04 pm. The (111) face, therefore, has a more open crystal structure in which the top 3 layers of atoms are exposed, as shown in the inset of **Figure 3.1A**. This results in surface Nb atoms being undercoordinated. Fully coordinated surface atoms are energetically favored, and the surface reconstructs and binds O to achieve full coordination. It was expected that long annealing times at temperatures in which surface atoms can overcome the energetic barrier to move to equivalent binding sites on the surface would improve long-range order; this was not observed, however, on Nb(111). In contrast, the Nb(100) face is more closely packed and exposes only the first two layers of Nb atoms (**Figure 3.1B**). As a result, Nb(100) exhibits more long-range order of the Nb(n×1)-O superlattice on Nb(100).

Because Nb(100) is a more well-defined surface than Nb(111) following UHV surface preparation, oxygen dissolution on oxidic Nb phases was studied utilizing the Nb(100) crystal. **Figure 3.2A** shows AES spectra of the Nb(100) crystal before (blue) and after (red) annealing (sample temperature, T_S) with the native oxide layer present to promote oxygen dissolution into the bulk metal. The principle Nb AES peak is at 169 eV while the O peak is at 519 eV. Following annealing, there is a significant decrease in the O peak at 519 eV and an increase in the Nb peak intensity at 169 eV. The room temperature O/Nb current intensity ratio (I_O/I_{Nb}) was observed to plateau at ≈ 0.2.

In order to determine the activation energy (E_A) for oxygen dissolution into the bulk, the

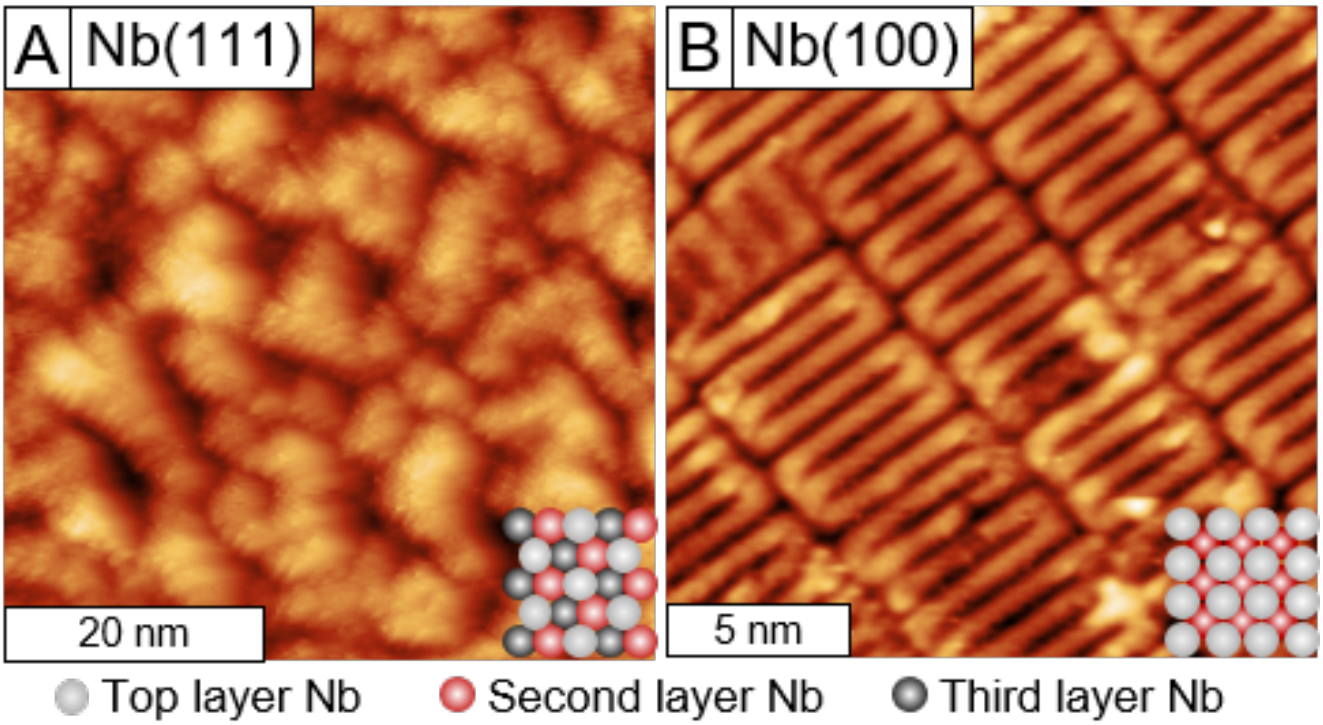

Figure 3.1: STM images show surface crystallographic orientation effects on NbO surface structure. **A:** V = - 0.5 V, I = - 0.1 nA. Nb(111) presents disordered oxide domains with no long-range order due to the open nature of the Nb(111) plane; **B:** V = -0.5 V, I = -19 pA. Nb(100) presents highly-ordered (n×1)-O superlattices due to the closely-packed Nb(100) plane.

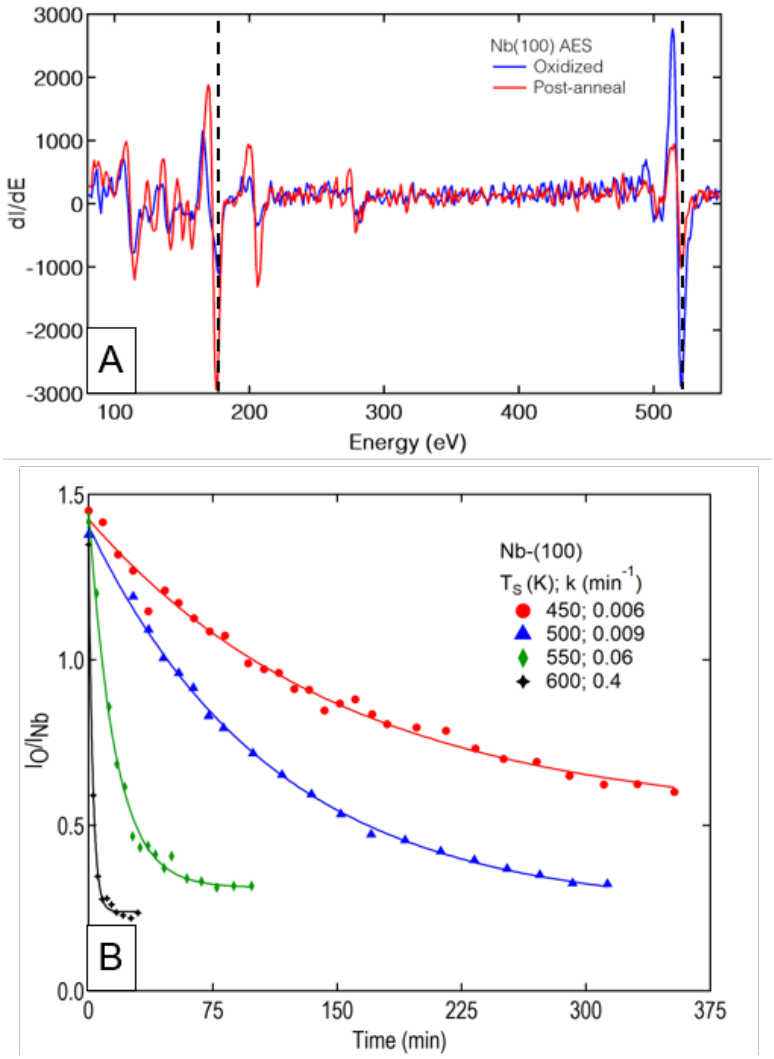

Figure 3.2: A: AES spectra before (blue) and after (red) and after annealing Nb(100) at 600 K. The principle Nb peak is located at 169 eV, and the O peak is at 519 eV, both indicated by dashed vertical lines in the plot. **B:** Ratio of O/Nb current intensity, I_O/I_{Nb}, vs. anneal length for various T_S. The height-to-height peak intensities of the oxygen to the niobium peak (factoring in standard correction factors for each element) were plotted for each AES scan as the measurements were continually taken while the crystal was held at the indicated temperature.

crystal was annealed at T_S = 450, 500, 550, and 600 K until the I_O/I_{Nb} value plateaued. As shown in **Figure 3.2B**, T_S = 450 K I_O/I_{Nb} stabilized after 350 min with I_O/I_{Nb} = 0.60, T_S = 500 K after 300 min with I_O/I_{Nb} = 0.32, T_S = 550 K after 100 minutes with I_O/I_{Nb} = 0.31, and T_S = 600 K after 25 minutes with I_O/I_{Nb} = 0.22. For T_S > 600 K, there was rapid oxygen dissolution, and while a final I_O/I_{Nb} = 0.22 was determined, sequential I_O/I_{Nb} values could not be obtained. Not only did lower T_S result in longer annealing times before I_O/I_{Nb} stabilized, but the amount of oxygen remaining on the surface was higher for lower T_S. This suggests that not only is the rate of oxygen dissolution dependent on T_S, but the oxidic phase present on the surface is in part determined by T_S. The activation energy, E_A, for O dissolution was determined to be 0.6 eV/atom (**Figure 3.3**). Previous work has indicated an E_A for oxygen removal, either *via* evaporation or surface-bulk diffusion, to be 0.74 eV/atom,[21] and is in agreement with our experimentally determined E_A of 0.6 eV/atom.

Following sputtering and annealing, Nb(100) was placed into the UHV-STM, and the (3×1)-O ladder structure was observed on all terraces of the Nb(100) surface, as shown in **Figure 3.4**. Further analysis of the parallel rows of (3×1)-O ladders shows that while the spacing between the ladders is a constant in the (3×1)-O structure, the widths of the ladders are not constant, and are rather distributed in a range of sizes. **Figure 3.5A** shows the statistical distribution of the periodic widths of the (3x1)-O ladder structures in units of the surface layer Nb-to-Nb interatomic distance (0.31 nm).[42] The distribution of the ladder widths is symmetric and centered around 10 Nb atoms. This is consistent with previously reported statistical analysis of the periodic widths of the (3x1)-O ladder widths on Nb(100).[33,37]

To characterize the structural evolution of the ladder structures as a result of oxygen dissolution, the (3x1)-O ladders were exposed to oxygen gas and annealed at 725 K to promote

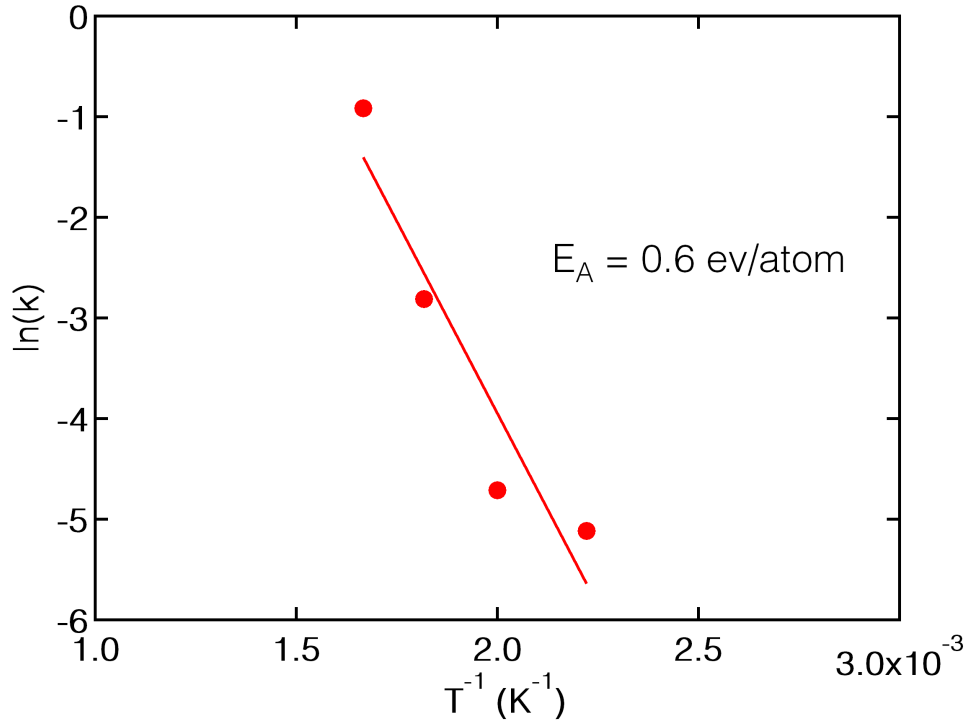

Figure 3.3: Arrhenius plot created using the temperature dependent rate constants from the dissolution trials in Figure 3.2. An activation energy for oxygen dissolution of 0.6 eV/atom was calculated.

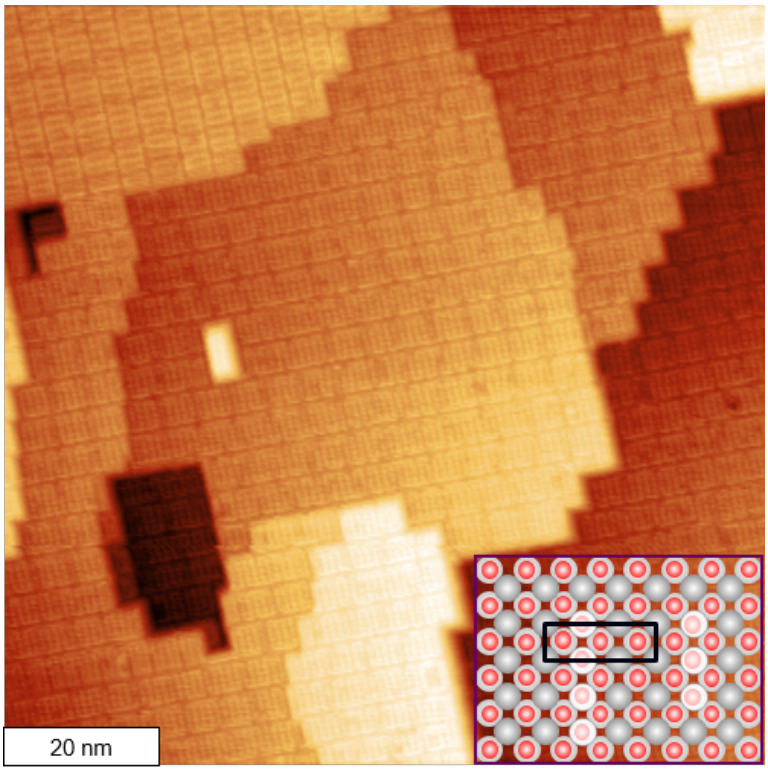

Figure 3.4: UHV-STM image (V = -0.5 V, I = - 19 pA) of the Nb(100) surface after Ar-ion sputtering and annealing at 1700 K with (3×1)-O schematic inset. Large, flat terraces displaying the (3×1)-O superlattice populate the entirety of the Nb(100) crystal. The (3x1)-O ladders are characterized by the spacing between the ladder rungs which is approximately 1.0 nm, or 3 times the niobium lattice parameter in the (100) plane. The widths of the ladders is not uniform but rather distributed in a range centered around a width equal to 10 Nb atoms (see Figure 3.5). This width is thought to be governed by the NbO/Nb lattice misfit.

oxygen dissolution but not regrow the ladder structures. This allowed us to make comparisons between the thermal annealed Nb(100) surface following oxygen dissolution to the initial, pristine Nb(100) (3×1)-O surface. The surface comprised of ladder structures in **Figure 3.5A** was exposed to 3.6 L O_2 at T_S = 300 K. This resulted in the chemisorption of oxygen atoms (O_{ad}) across the NbO surface oxide with no incorporation of oxygen into the ladder structure nor evolution of the underlying ladder structure, as seen in **Figure 3.5B**. Statistical analysis was performed on the ladder structures in **Figure 3.5B** to confirm that the underlying surface structure of the ladders had not been altered, and similar to the distribution of ladder widths in **Figure 3.5A**, the majority of ladders were 10 Nb atoms wide. After confirming that the chemisorption of O_{ad} did not perturb the underlying (3×1)-O ladder structure, the surface was annealed at T_S = 725 K for 20 minutes to promote the dissolution of chemisorbed oxygen through the ladder structures into the Nb bulk as shown in **Figure 3.5C**. The ladder structures, while still present, have begun to break apart as a result of oxygen dissolution into the bulk of the Nb crystal. The ladders are now interrupted with dark pits on the surface, consistent with more extensive oxidation, and ladder rungs are segmented into smaller ladder fragments. Visually, there is a marked decrease in overall ladder domain order compared to the pristine ladder surface in **Figure 3.5A**. A histogram of the periodic ladder lengths, shown in the histogram inset of **Figure 3.5C**, confirms the evolution of the ladder widths, with a larger portion of the Nb surface comprised of narrower ladder features. While there are still 10 Nb atom wide ladders present on the surface, a significant portion of the ladders have been disrupted by the oxygen dissolution and a noticeable increase in narrower ladder widths are observed. Following the 20 min anneal at T_S = 725 K, the surface was annealed for an additional 20 min, resulting in a total anneal time of 40 min. **Figure 3.5D** shows the continued surface evolution following the 40 min total anneal at T_S = 725 K. In addition to the dark pits consistent with

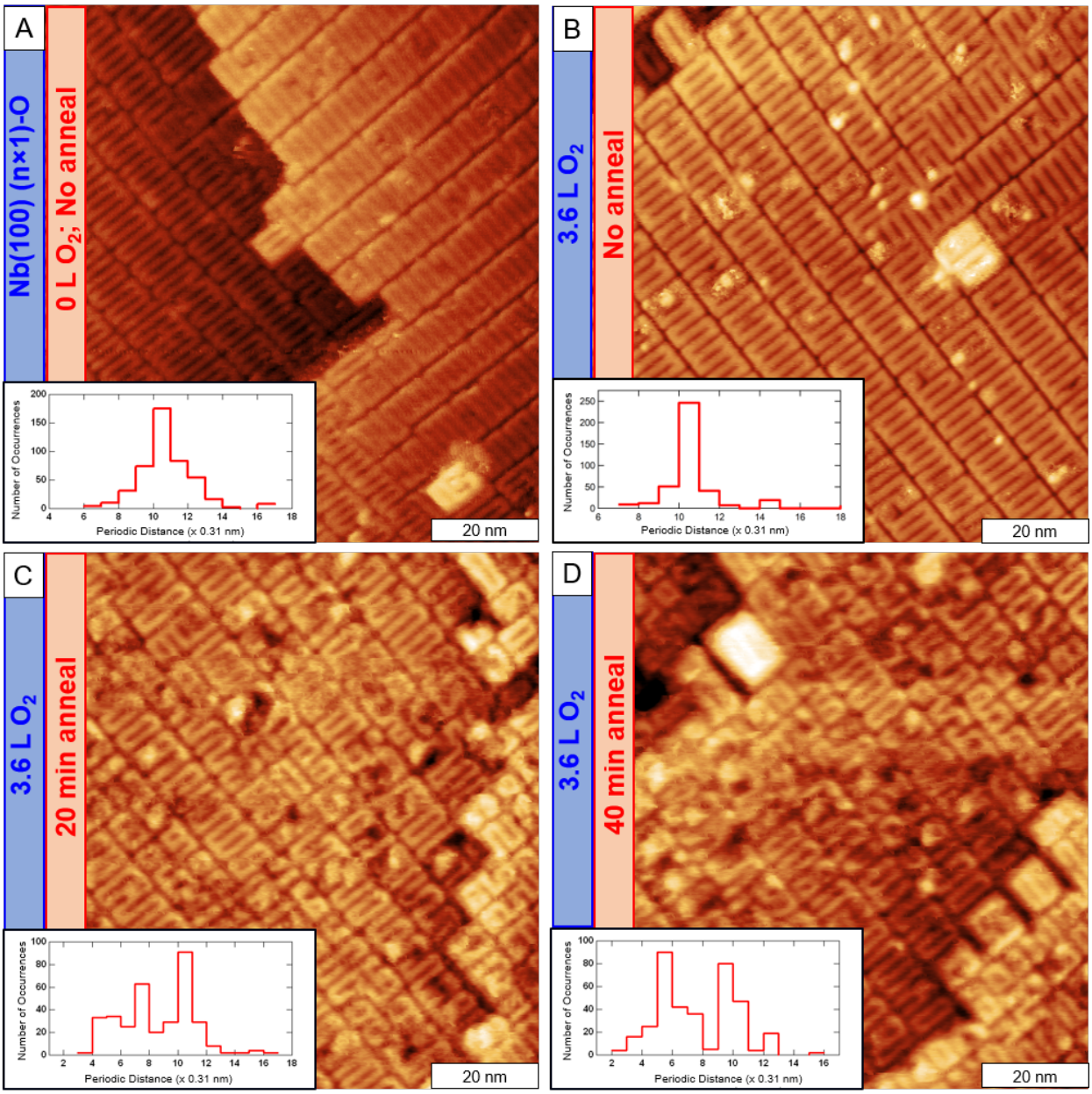

Figure 3.5*:* STM images of the Nb(100) (3×1)-O surface after two subsequent doses of 3.6 L of oxygen gas at T_C =300 K and subsequent annealing at 725 K. **A:** Pristine (3×1)-O surface and ladder width histogram; **B:** (3×1)-O surface with chemisorbed O_{ad} following a 3.6 L O_2 exposure with no anneal; **C:** (3×1)-O surface with 3.6 L O_2 annealed at 725 K for 20 min total and ladder width histogram; **D:** (3×1)-O surface with 3.6 L O_2 annealed at 725 K for 40 min total and ladder width histogram. Imaging conditions: A) V = - 0.5 V, I = - 19 pA; B) V = -0.5 V, I = -18 pA; C) V = - 0.51 V, I = -19 pA D) V = - 0.51 V, I = -18 pA.

further surface oxidation as was shown in **Figure 3.5C**, there are small areas where no ladder pattern is discernable. Additionally, there is an increase in the occurrence of narrow ladder widths compared to **Figure 3.5A-C**, as seen in the histogram inset of **Figure 3.5D**. The most frequent ladder width in **Figure 3.5D** has also shifted from 10 Nb atoms to 9, consistent with continual surface evolution as the oxygen dissolution disrupts the original pristine ladders as it diffuses into the bulk. It is interesting to note the frequent occurrence of 5 Nb atoms in this histogram inset of **Figure 3.5D**, which is half of the unperturbed ladder length of 10 Nb atoms. This could indicate a preferred location for O_{ad} penetration into the bulk at the center point of the existing ladder rungs. Following the extensive anneal at T_S = 725 K, the surface was annealed further above T_S = 900 K, and the pristine (3×1)-O surface was restored.

These surface reconstructions provide the first detailed visualization of changes to the Nb(n×1)-O superlattice on Nb(100) that result from chemisorbed O_{ad} dissolving into the bulk. This is important for understanding the changes that occur at the oxide/metal interface during mild bake treatments to improve SRF cavity performance, contaminant and dopant incorporation into the Nb bulk, and the growth of thin films on oxide covered niobium to improve SRF performance with next generation superconducting alloys such as Nb_3Sn. Future studies will combine these results with first principles calculations to develop an atomic scale model for oxygen dissolution and mass transport through the Nb(100) (3×1)-O ladder structures.

3.4 Conclusion

To elucidate the energetics of oxygen dissolution through relevant (3×1)-O ladder structures on Nb(100) and subsequent atomic-scale structural evolution as a result of oxygen dissolution, the (3×1)-O ladder structure on Nb(100) was studied with AES and STM following

thermal annealing to provide ensemble chemical and local structural information of the Nb surface. The (111) and (100) faces of Nb were used as model systems to investigate differences in surface oxide ordering, and it was discovered that the Nb(100) surface forms (3×1)-O ladder structures with large, ordered domains while the Nb(111) surface oxide does not form long-range order despite extended high temperature thermal annealing. Surface reconstructions of the Nb(100) (3×1)-O surface were observed as a result of oxygen dissolution into the bulk, and these results provide a detailed visualization of the changing structure of the oxide/metal interface during oxygen dissolution promoted by mild heat treatments of the niobium metal. In addition, the rate for oxygen dissolution was determined across a range of temperatures yielding an activation energy for oxygen dissolution of 0.6 eV/atom. This work provides real-space structural information regarding the complex surface evolution of Nb oxide as a function of thermal annealing, and has significant implications for actual SRF cavity fabrication processes. The importance of Nb oxide structure and chemical composition dictates the efficacy of beneficial dopant incorporation, the formation of high Q thin films such as Nb_3Sn, and the overall performance of SRF cavities under operating conditions. By increasing our understanding of the fundamental energetics and structural evolution of the Nb(100) (3×1)-O surface during oxygen dissolution, the opportunity to optimize Nb SRF cavity fabrication for increased particle accelerator facility performance may be realized.

3.5 Copyright Permissions

The data presented in this chapter was previously published in Surface Science. The following content was reprinted with permission from [R. Darren Veit, Natalie A. Kautz, Rachael

G. Farber, and S.J. Sibener, "Oxygen Dissolution and Surface Oxide Reconstructions on Nb(100)" Surface Science, DOI: 10.1016/j.susc.2019.06.004 (2019).] Copyright 2019, Elsevier.

3.6 Acknowledgments

This work was supported by the U.S. National Science Foundation under Award PHY-1549132, the Center for Bright Beams. Preliminary work was supported by the U.S. National Science Foundation under Award PHY-1535639. R.D.V. thanks Fermi National Accelerator Laboratory and The University of Chicago for partial fellowship support during this work.

3.7 References

1. Padamsee, H. *RF Superconductivity.* Wiley-VCH: Weinheim, 2009; p 159.
2. Ford, D.C.; Cooley, L.D.; Seidman, D.N. Suppression of hydride precipitates in niobium superconducting radio-frequency cavities. *Superconductor Science Technology*, **2013,** *26,* 105003.
3. Ford, D.C.; Cooley, L.D.; Seidman, D.N. First-principles calculations of niobium hydride formation in superconducting radio-frequency cavities. *Superconductor Science Technology*, **2013,** *26,* 095002.
4. Barkov, F.; Romanenko, A.; Trenikhina, Y.; Grassellino, A. Precipitation of hydrides in high purity niobium after different treatments. *Journal of Applied Physics*, **2013,** *114,* 164904.
5. Tao, R.; Romanenko, A.; Cooley, L.D.; Klie, R.F. Low temperature study of structural phase transitions in niobium hydrides. *Journal of Applied Physics*, **2013,** *114,* 0443606.

6. Romanenko, A.; Barkov, F.; Cooley, L.D.; Grassellino, A.. Proximity breakdown of hydrides in superconducting niobium cavities. *Superconductor Science and Technology*, **2013,** *26,* 035003.
7. Romanenko, A.; Grassellino, A.; Barkov, F.; Ozelis, J.P. Effect of mild baking on superconducting niobium cavities investigated by sequential nanoremoval. *Physical Review Special Topics – Accelerators and Beams*, **2013,** *16,* 012001.
8. Grassellino, A.; Romanenko, A.; Sergatskov, D.; Melnychuk, O.; Trenikhina, Y.; Crawford, A.; Rowe, A.; Wong, M.; Khabiboulline, T.; Barkov, F. Nitrogen and argon doping of niobium for superconducting radio frequency cavities: A pathway to highly efficient accelerating structures. *Superconducting Science Technology*, **2013,** *26,* 102001.
9. Ciovati, G. Review of the Frontier Workshop and Q-slope Results. *Physica C,* **2006,** *441,* 44-50.
10. Greenwood, N.; Earnshaw, A. *Chemistry of the Elements,* 2nd Ed. Butterworth-Heinemen: Oxford, 1997, pp 982-83.
11. Farrell, H.H.; Strongin, M. Interaction of oxygen and nitrogen with Nb(100) surface: Morphology. *Surface Science,* **1973,** *38,* 18-30.
12. Farrell, H.H.; Strongin, M, Interaction of oxygen and nitrogen with Nb(100) surface: Reaction-kinetics. *Surface Science,* **1973,** *38,* 31-52.
13. Pantel, R.; Bujur, M.; Bardolle, J. Continuous measurement of surface-potential variations during adsorption of (100), (110) and (111) faces of Nb using mirror electron microscope. *Surface Science*, **1977,** *62,* 589-609.
14. Usami, S.; Tominaga, N.; Nakajima, T. AES-LEED Study of Adsorption of Common Gases on the (100) planes of W and Nb. *Vacuum*, **1977,** *27,* 11.

15. Dawson, P.H.; Tam, W.C. The Interaction of Oxygen with Polycrystalline Niobium Studied Using AES and Low-Energy SIMS. *Surface Science*, **1979,** *81,* 464.

16. Rieder, K.H. On the Interaction of Oxygen with Nb(110) and Nb(750). *Appl. Surf. Sci.*, **1980,** *4,* 183.

17. Hu, X.P.; Li, Y.P.; Ji, M.R.; Hu, J.X. The Interaction of Oxygen with Niobium Studied by XPS and UPS. *Solid State Commun.*, **1989,** *71,* 849.

18. Sanz, J.M.; Hoffman, S. Auger Electron Spectroscopy and X-Ray Photoelectron Spectroscopy Studies of the Oxidation of Polycrystalline Tantalum and Niobium at Room Temperature and Low Oxygen Pressures. *Journal of the Less-Common Metals*, **1983,** *92,* 317-327.

19. Lindau, I.; Spicer, W.E. Oxidation of Nb as Studied by UV-Photoemission Technique. *J. Appl. Phys.*, **1974,** *45,* 3720.

20. Wang, Y.; Wei, X.; Tian, Z.; Cao, Y.; Zhai, R.; Ushikubo, T.; Sato, K.; Zhuang, S. An AES, UPS, and HREELS Study of the Oxidation and Reaction of Nb(110). *Surface Science*, **1997,** *372,* 285.

21. Franchy, R.; Bartke, T.U.; Gassmann, P. The interaction of oxygen with Nb(110) at 300, 80 and 20 K. *Surface Science*, **1996,** *366,* 60-70.

22. Fromm, E.; Jehn, H. Thermodynamics and Phase Relations in Refractory Metal Solid Solutions Containing Carbon, Nitrogen, and Oxygen. *Metallugical Transactions*, **1972,** *3,* 1685-1692.

23. Rovner, L.H.; Drowart, A.; Degreve, F.; Drowart, J. Air Force Materials Laboratory Technical Report AFML-TR-68-200, July 1968.

24. Pasternak, R.A.; Evans, B. Adsorption, Absorption, and Degassing in the Oxygen-Niobium System at Very Low Pressure. *J. Electrochem. Soc.* **1967,** *114,* 452-457.

25. Oechsner, H.; Giber, J.; Füber, H.J.; Darlinski, A. *Thin Solid Films*, **1985,** *124,* 199.

26. Hörz, G. Mechanisms and Kinetics of Absorption and Desorption Reactions in Systems of Refractory Metals with Nitrogen, Oxygen, and Carbon. *Metallurgical Transactions*, **1972,** *3,* 3069.

27. Lo, W.S.; Chen, H.H.; Chien, T.S.; Tsan, C.C.; Fang, B.S. Oxidation of Nb(001) studied by high-resolution core-level photoemission. *Surface Review and Letters*, **1997,** *4,* 651-654.

28. Daccà, A.; Gemme, G.; Mattera, L.; Parodi, R. *Applied Surface Science,* **1998,** *126,* 219.

29. King, B.R.; Patel, H.C.; Gulino, D.A.; Tatarchuk, B.J. Kinetic Measurements of Oxygen Dissolution into Niobium Substrates: *In-situ* X-ray Photoelectron Spectroscopy Studies. *Thin Solid Films*, **1990,** *192,* 351-369.

30. Arfaoui, I.; Guillot, C.; Cousty, J.; Antoine, C. Evidence for a Large Enrichment of Interstitial Oxygen Atoms in the Nanometer-Thick Metal Layer at the NbO/Nb(110) Interface. *Journal of Applied Physics,* **2002,** *91,* 9319.

31. Arfaoui, I.; Cousty, J.; Guillot, C. A model of the NbO nanocrystals tiling a Nb(110) surface annealed in UHV. *Surface Science,* **2004,** *557,* 119–128.

32. Sürgers, C.; Schöck, M.; Löhneysen, H. Oxygen-induced surface structure of Nb(110). *Surface Science,* **2001,** *471,* 209–218.

33. Uehara, Y.; Fujita, T.; Iwami, M.; Ushioda, S. Single NbO Nano-Crystal Formation on Low Temperature Annealed Nb(001) Surface. *Surface Science,* **2000,** *472,* 59.

34. Li, Y.; An, B.; Xu, X.; Fukuyama, S.; Yokogawa, K.; Yoshimura, M. Surface structure of niobium- dioxide overlayer on Nb(100) identified by scanning tunneling microscopy. *Journal of Applied Physics,* **2001,** *89,* 4772–4776.

35. An, B.; Fukuyama, S.; Yokogawa, K.; Yoshimura, M. .Surface structures of clean and oxidized Nb(100) by LEED, AES, and STM. *Physical Review B,* **2003,** *68,* 115423.

36. Li, T.; An, B.; Fukuyama, S.; Yokogawa, K.; Yoshimura, M. Surface oxidation of a Nb(100) single crystal by scanning tunneling microscopy. *Materials Characterization,* **2002,** *48,* 163–167.

37. Razinkin, A.S.; Kuznetsov, M.V. Scanning tunneling microscopy (STM) of low-dimensional NbO structures on the Nb(110) surface. *Physics of Metals and Metallography,* **2010,** *110,* 531-541.

38. Kuznetsov, M.V.; Razinkin, A.S.; Ivanovskii, A.L. Oxide nanostructures on an Nb surface and related systems: Experiments and *ab initio* calculations. *Physcis – Uspekhi,* **2010,** *53,* 995-1014.

39. Kuznetsov, M.V.; Razinkin, A.S.; Shalaeva, E.V. Photoelectron spectroscopy and diffraction of surface nanoscale NbO/Nb(110) structures. *Journal of Structural Chemistry,* **2009,** *50,* 514-521.

40. Shein, K.I.; Shein, I.R.; Medvedeva, N.I.; Shalaeva, E.V.; Kuznetsov, M.V.; Ivanovskii, A.L. Effects of atomic relaxation and the electronic structure of niobium (100) and (110) surfaces. *Physics of Metals and Metallography,* **2006,** *102,* 604-610.

41. Wen, M.; An, B.; Fukuyama, S.; Yokogawa, K. First-Principles Study of Oxidized of Nb(100) Surface Structures. *Surface Science*, **2009,** *603,* 216-220.

42. Tafen, D.N.; Gao, M.C. Oxygen atom adsorption on and diffusion into Nb(110) and Nb(100) from first principles. *JOM,* **2013,** *65,* 1473-1481.

43. Wang, G.Q.; Shang, J.X.; Yang, Z. First-Principles study on the initial oxidization of Nb(100). *Journal of Physical Chemistry C,* **2012,** *116,* 23371-23376.

44. Wang, G.Q.; Shang, J.X. First-principles study on the incipient oxidization of Nb(110). *Journal of Physics: Condensed Matter,* **2012,** *24,* 225005.

45. Wells, A.F., *Structural Inorganic Chemistry*, Oxford University Press: London, 1962, *457,462,967,1021*.

Chapter 4: Nano-Scale Characterization of Niobium Hydride Growth and Suppression Behavior on Nb(100)

4.1 Introduction

Particle accelerators, commonly associated with fundamental particle physics research, are crucial to scientific progress in fields including materials science and biology as well as in industrial and medical applications. Superconducting radio frequency (SRF) cavities provide longitudinal acceleration to a beam of charged particles,[1,2] and are a crucial component of high efficiency linear particle accelerators. Improving and optimizing the performance of SRF cavities, therefore, is necessary when building and upgrading state-of-the-art accelerator facilities. The current standard for SRF cavities is niobium (Nb) which has a critical temperature (T_c) of 9.25 K.[2–4] Niobium is the highest performing elemental superconductor due to its ultra-low surface resistance (R_s) and high quality factor (Q) at operating temperatures of ~ 2 K.[1] The chemical and structural composition of the Nb SRF cavity surface is crucial; the penetration depth of the electromagnetic field is ~ 100 nm and limiting structural and chemical features that decrease Q is essential. As a result of this strong dependence on surface properties and Q, previous work has investigated the relationship between surface morphology,[3,5-7] defects,[8–11] and contaminant incorporation[8-10] on the superconducting properties of Nb SRF cavities, as well as developing processing procedures to improve cavity performance.[3,11]

One of the most significant sources of SRF cavity performance losses is the presence of hydrogen within the Nb bulk which precipitates as Nb hydrides upon cooling to operating temperatures of ~ 2 K.[12-14] Nb readily absorbs hydrogen when the bulk oxide Nb_2O_5 is removed from the surface.[12,14] During cavity fabrication, the cavity surface is polished via either buffered chemical polishing (BCP), electropolishing (EP), or centrifugal barrel polishing (CBP). These

procedures continuously strip away the native surface oxide layer, allowing for the absorption of significant amounts of hydrogen into the Nb cavities.[15] At room temperature, the absorbed hydrogen occupies interstitial sites in the near surface and bulk of the Nb cavity.[13] As the cavity is cooled, however, the hydrogen precipitates into Nb hydrides that populate the cavity surface as micron-scale Nb hydrides with nucleation and growth temperatures between ~70 K and 170 K.[12,14] These Nb hydride species are non-superconducting at $T > 1.3$ K[13], and the presence of Nb hydrides results in a significant decrease of cavity Q and performance due to local surface heating; this has phenomenon has been dubbed the "hydrogen Q disease".[16-18]

While degassing the cavities under ultra-high vacuum (UHV) conditions at 1100 K considerably reduces the observed effects of hydrogen Q disease, there remains a significant concentration of absorbed hydrogen that precipitates as smaller, nano-scale hydride species.[12-14] Recent work has demonstrated that a nitrogen doping step following hydrogen degas in UHV reliably increases Q, and reverses the Q field dependence in the medium field regime.[8,10,19,20] Point contact tunneling spectroscopy (PCTS) measurements performed on conventionally processed and nitrogen doped SRF cavity coupons have shown that the conventionally processed cavities exhibit local hotspots of decreased superconductivity, which are consistent with the presence of Nb hydride species. PCTS measurements of these hot spots display a narrowed superconducting gap (Δ) at high RF fields where Q losses generally occur, consistent with increased surface resistance and local surface heating. Inhomogeneity in surface temperature was observed, and unaffected cold regions displaying standard Δ were seen to coexist with Nb hydride regions.[21] Nitrogen doped cavities exhibit a more homogeneous gap distribution with fewer hotspots present to indicate the presence of Nb hydrides. The reduced occurrence of hotspots on the nitrogen doped cutouts, and the lack of a narrowed Δ indicates that nitrogen plays a role in preventing Nb hydride phases from

nucleating and growing in the near-surface region. This is supported by first principles calculations showing that nitrogen interstitials can increase the barrier to hydrogen diffusion between tetrahedral sites, effectively trapping hydrogen in the bulk and preventing Nb hydride precipitation.[20]

Despite the work done to identify the effects of hydrogen and nitrogen on Nb SRF cavities, little is understood regarding the incipient, nano-scale growth and structural evolution of Nb hydrides or how nitrogen infusion disrupts this process. In this work we have used Nb(100) as a model system to investigate the initial nano-scale structural evolution of Nb(100) as a function of Nb hydride precipitation in real time using low-temperature scanning tunneling microscopy (LT-STM). Additionally, the unique electronic characteristics of hydride phases have been characterized using scanning tunneling spectroscopy (STS) and supported via DFT surface bandgap calculations. We then demonstrated the successful suppression of Nb hydrides following the co-infusion of nitrogen and hydrogen in Nb(100), and elucidated unique electronic characteristics due to the presence of both nitrogen and hydrogen in the near surface of Nb(100) which were supported via DFT surface bandgap calculations. These results provide novel information regarding the initial, nano-scale structural and electronic evolution of Nb(100) as a result of Nb hydride growth and nitrogen-induced hydride suppression.

4.2 Experimental

Experiments were performed in a UHV chamber comprised of a preparation chamber and scanning tunneling microscopy chamber (UHV VT-STM, RHK Technology, Try, MI) with the Nb(100) crystal (Surface Preparation Laboratory, Zaandam, NL) mounted on a custom RHK six-contact sample puck, as previously described.[22] The preparation chamber, which has a base

pressure of $\leq 1.0\times10^{-10}$ torr, contains Auger electron spectroscopy (AES), x-ray photoelectron spectroscopy (XPS), and Ar^+ ion sputtering capabilities, as well as a residual gas analyzer (RGA). The crystal was cleaned via cycles of Ar^+ ion sputtering and annealing at 2100 K, measured using an infrared pyrometer (Mikron Infrared, MG-140) mounted outside of the UHV chamber. Surface cleanliness was confirmed with AES, XPS, and STM analysis.

Hydrogen and nitrogen exposures and temperature programmed desorption measurements were carried out in the preparation chamber. The surface was first prepared in the manner described previously to produce the (3x1)-O ladder structures. To produce the hydrogen doped surface, after the 2100 K anneal to produce the ladders, the temperature of the crystal was reduced to and held at 800 K. The chamber was then backfilled to 5.5×10^{-5} Torr hydrogen *via* a leak valve on the chamber. After 20 minutes, the gas was shut off, the heating of the crystal was shut off, and the crystal was transferred to the microscope chamber where it was allowed to equilibrate overnight before beginning STM measurements the following day. At the conclusion of the STM and STS measurements, the crystal was returned to the preparation chamber where a TPD was performed to capture the hydrogen desorption peak. The temperature was ramped from 800 K to 1200 K with the e-beam heater. Mass channel 2 was monitored with the residual gas analyzer to capture the hydrogen desorption peak. Mass channel 28 was also monitored for consistency with TPDs from the co-doped crystals. Hydrogen TPDs taken prior to the STM experiments were identical to those taken after completion of the STM experiments; there was no evidence of background gas accumulation or surface degradation.

To produce the nitrogen and hydrogen doped surface, the crystal temperature was reduced to and held at 1100 K after the 2100 K anneal. 1100 K was chosen because it is the temperature at which Nb SRF cavities are doped with nitrogen. The chamber was then backfilled to 20 mtorr

nitrogen *via* the same prep chamber leak valve. After ten minutes the gas was shut off. The temperature of the crystal was maintained at 1100 K while the nitrogen tank was switched out for the hydrogen tank. The machine, at the time of these experiments, was not equipped with a gas manifold that allows for multiple tanks to be attached to the foreline simultaneously. Let it be noted that a gas manifold would have been very helpful and should be installed in the future. After the hydrogen was attached, the temperature of the crystal was reduced to and held at 800 K again for the hydrogen doping. Through repeated trials of doping the crystal, it was determined that the nitrogen absorption has a slight effect on the hydrogen absorption. For this reason, in order to infuse the same amount of hydrogen into the crystal for both the hydrogen only experiments and the co-doped experiments, the chamber was backfilled to 1.0×10^{-4} Torr hydrogen after nitrogen absorption had taken place. This produced an identical desorption peak integration to the hydrogen only procedure. The nitrogen doping step must be performed first when preparing the co-doped surface because hydrogen desorbs from the bulk at the temperature at which the nitrogen doping is performed. The gas was shut off after twenty minutes, the heating of the crystal was shut off, and the crystal was transferred to the microscope chamber to equilibrate overnight for STM measurements the next day. At the conclusion of the STM and STS measurements, the crystal was returned to the preparation chamber for TPD measurements. Temperature ramps of 800 K to 1200 K and 800 K to 2100 K were performed to capture both the hydrogen desorption and the nitrogen desorption events, which desorb at different temperatures. Both mass channels 2 and 28 were monitored with the residual gas analyzer during both temperature ramps. TPDs for the co-doped crystals also showed no difference between those performed prior to STM experiments and those performed after completion.

STM and STS data was collected using the Beetle-style VT-STM cooled with the continuous flow liquid helium cryostat described earlier to maintain an STM stage temperature (T_{STM}) of 100 K. This temperature was chosen because it is well known that hydrides precipitate between 70 K and 170 K, and that the most dangerous temperature zone within this range is between 90 K and 130 K. 100 K is both in this range and an easily achievable temperature by simply controlling the flow of the liquid helium in the flow cryostat. dIdV was measured with an external lock-in amplifier (Stanford Research Systems, SR830 DSP). Typical settings for dIdV measurements were as follows: pre-sample delay: 0.10 ms, sampling time: 10.00 ms, lock-in time constant: 3 ms, modulation bias amplitude: 40-60 mV, modulation bias frequency: 1 kHz. The bias was typically swept between -3.00 to 3.00 V, with an energy step size of 50.00 mV. This bias window and step size were chosen because they captured the bandgap with adequate resolution and produced IV curves in a reasonable amount of time. The bias range and energy resolution are adjustable in the software settings for the RHK electronics. There was no difference in bandgap observed for reasonable adjustments to the resolution or bias range given that an appropriate range for capturing the bandgap was chosen. Care must be taken in finding the appropriate spectroscopy and lock-in settings in order to obtain high quality data. The modulation bias amplitude must be high enough to get a signal but not too high to introduce noise into the measurement. 40-60 mV was typically found to be an ideal amplitude. The modulation frequency must be high enough to not interfere with the measurement. The pre-sample delay is chosen to give the lock-in amplifier sufficient time to stabilize before taking the measurement. The sampling time must be high enough to obtain a sufficient signal-to-noise ratio but not too high as to where thermal drift affects the measurement. The time constant of the lock-in must be chosen to optimize the stability and

responsivity of the lock-in output. Optimal parameters are typically determined through adjustments during data acquisition.

4.3 Results and Discussion

The Nb(100) (3×1)-O NbO ladder structures that have been described in detail in previous work[22,24] are used as a benchmark for surface structural evolution as a function of Nb hydride growth in this work. Without exposure to hydrogen, the blank Nb(100) crystal shows no appreciable hydrogen or nitrogen desorption feature when either of the temperature ramps discussed in the experimental section are performed, as can be seen in **Figure 4.1a**. Following hydrogen exposure, there is a significant hydrogen desorption feature while no nitrogen desorption feature is observed, as can be seen in the TPD spectra in **Figure 4.1b**. After the nitrogen doping and hydrogen doping the same crystal, both desorption peaks are observed, the hydrogen during the first temperature ramp, and the nitrogen during the second temperature ramp, as can be seen in **Figure 4.1c**. It is interesting to note that there is significantly less nitrogen incorporated than hydrogen. This is in agreement with recent SIMS results that show a very small concentration of nitrogen in the first few nanometers of the Nb cavity coupons.[24,25] Given the diffusion constant of nitrogen in Nb at 1100 K, the thickness of our Nb(100) crystal, and assuming that hydrogen is dispersed equally throughout the bulk, we can estimate that there is within the same order of magnitude equal parts nitrogen and hydrogen within the nitrogen diffusion depth. These TPDs demonstrate that we have developed a doping procedure that incorporates consistent amounts of both hydrogen and nitrogen into our Nb(100) crystal to study both hydride growth and suppression behavior with the STM.

After developing a consistent doping procedure, the different surfaces were characterized with the STM at room temperature to compare to the blank (3x1)-O surface. Room temperature STM images of the undoped, hydrogen doped, and hydrogen and nitrogen doped Nb(100) (3x1)-O surface are shown in **Figure 4.2**. **Figure 4.2a** shows the pristine Nb(100) (3x1)-O surface following standard UHV cleaning procedures.[22] These are the blank ladders described throughout this thesis. Following hydrogen incorporation, there is no evidence of perturbation to the (3×1)-O ladder structures during STM experiments, as shown in **Figure 4.2b**. STM imaging of the hydrogen and nitrogen infused surface, seen in **Figure 4.2c**, does show perturbation to the native (3×1)-O NbO surface. This perturbation may be due to substitution of surface oxygen with nitrogen in the NbO lattice, resulting in the dark patches seen in the ladders; such substitutional behavior is energetically favorable as predicted by DFT calculations from our collaborators in the Arias Group.

To obtain structural and electronic information regarding the initial nano-scale growth and suppression mechanisms of Nb hydrides with and without nitrogen incorporation, time-lapse LT-STM was employed to observe real-time structural evolution while T_{sample} = 100 K; this choice of T_{sample} was explained earlier and is within the nucleation and growth range of Nb hydrides.[12,14] Upon cooling and equilibration at the STM temperature (T_{STM}) of 100 K, STM measurements taken within hours of reaching equilibrium for the undoped (**Figure 4.3a**), hydrogen doped (**Figure 4.3b**), and nitrogen and hydrogen doped (**Figure 4.3c**) Nb(100) crystal show no surface evolution compared to each respective sample preparation at room temperature.

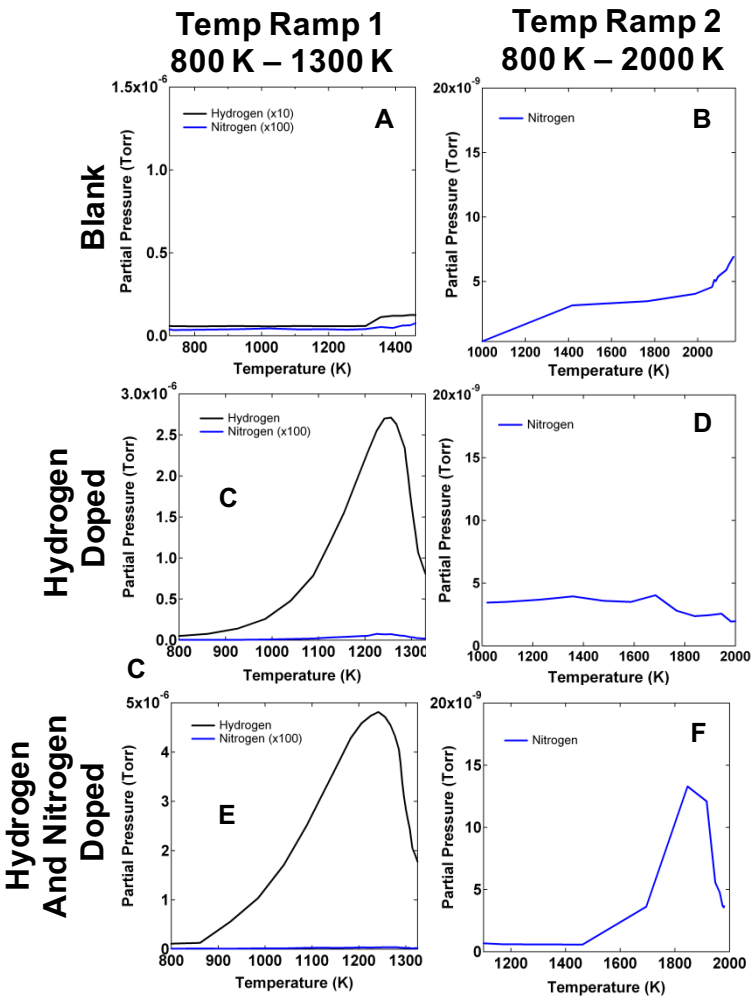

Figure 4.1: TPD spectra of Nb(100) (3x1)-O using two separate temperature ramps to capture both the hydrogen and nitrogen desorption peaks on all of the blank, hydrogen doped, and nitrogen and hydrogen doped crystals. Doping parameters were as follows: **A,B** (blank): without exposure to hydrogen or nitrogen, and no evidence of absorbed nitrogen or hydrogen; **C,D** (hydrogen doped): exposure to 5.5×10^{-5} Torr hydrogen with the sample at T_{sample} = 800 K for 20 minutes; **E,F** (nitrogen and hydrogen doped): 2×10^{-2} Torr nitrogen at T_{sample}= 1100 K for 10 minutes followed by exposure to 1.0×10^{-4} Torr hydrogen with the sample at T_{sample} = 800 K for 20 minutes. These TPDs demonstrate consistent and reliable doping procedures for incorporating both hydrogen and nitrogen into the Nb(100) crystal to study both hydride growth and suppression behavior.

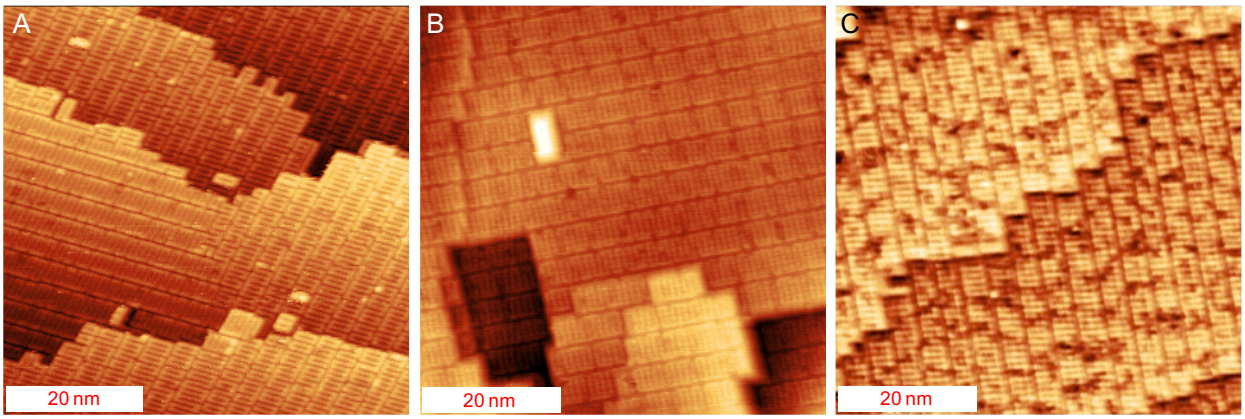

Figure 4.2: Room temperature STM images of Nb(100) (3x1)-O following **A:** No dopant incorporation with pristine (3x1)-O ladders covering the surface; **B:** Exposure to 5.5×10^{-5} Torr hydrogen with the sample at T_{sample} = 800 K for 20 minutes. No evidence of surface perturbation following the hydrogen exposure is observed, and the surface is covered in pristine (3x1)-O ladders; **C:** Exposure to 2×10^{-2} Torr nitrogen at T_{sample}= 1100 K for 10 minutes followed by hydrogen incorporation. Following nitrogen incorporation, there is noticeable perturbation of the (3x1)-O ladder structure. Dark features appear sporadically across the surface, and suggest nitrogen incorporation into the NbO surface oxide. Imaging conditions A) 0.72 V, 99 pA; B) 181 mV, 178 pA; C) -406 mV, 179 pA

Additionally, the STS surface bandgap data for each sample preparation within several hours of equilibration at T_{STM} = 100 K shows no deviation from the undoped Nb(100) (3x1)-O surface bandgap (**Figure 4.2d**). The absence of structural evolution coupled with a consistent surface bandgap across all sample preparations suggests that no Nb hydride growth had begun within this time frame. Nb hydrides grow rapidly within the nucleation range of ~ 100 K to 170 K over the course of hours on polycrystalline Nb cavity coupons[14] due to bulk and surface defects that serve as nucleation sites for Nb hydrides, and grain boundaries that provide for rapid transport from the bulk to the surface.[26,27] The lower defect density in Nb(100) results in significantly slower nucleation and growth rate of Nb hydrides on Nb(100) due to the lack of nucleation sites and grain boundaries on the single crystal surface. As such, the absence of surface evolution due to Nb hydride growth and no evidence of attenuation of the surface bandgap is not unexpected.

In order to capture the hydride growth behavior, an area on the hydrogen doped surface was continuously imaged in the same location for over 72 hours. A series of STM and STS measurements depicting this timeline of events is shown in **Figure 4.4a-f**. An area with distinct facets, as shown in the STM images in **Figure 4.4a,d,e,f**, was selected for time-lapse imaging to serve as a positional reference point during surface evolution; the lateral surface evolution occurs at very large time scales and the static facets serve to ensure thermal drift is not contributing to the observed structural evolution. An STM image of the area exhibiting distinct facets after 24 hours of cooldown is shown in **Figure 4.4a**, with the blank bandgap measured on all terraces and facets as shown in **Figure 4.4b**. The stars in **Figure 4.4a** correspond to the measured STS location in **Figure 4.4b**. After 24 hours, it is clear that no change to the surface bandgap has occurred. **Figure 4.4c** shows a linescan depicting the sharp facet on the surface seen in the STM image in **Figure 4.4d**. As stated, this facet will serve as an essential reference point for observing the surface

structural evolution that is depicted in **Figure 4.4d-e**. **Figure 4.4d-e** depicts lateral surface evolution of the terraces and etch pits over a 16-hour overnight time lapse on the hydrogen infused surface. Relevant step edges and etch pits are masked in blue to assist the eye. Following the overnight scan (**Figure 4.4e**), the step edges and etch pits can be seen to retreat relative to the facet, depicted by the blue arrows in **Figure 4.4d-e**. Nb atoms do not move translationally without significant perturbation at 100 K, so the observed surface evolution is concluded to be a consequence of the growth of hydride phases in the near surface.

The surface bandgap was measured *via* dIdV following the time-lapse imaging sequence, after 72 hours of cooldown, as shown in **Figure 4.4f-g**. The blank bandgap was no longer measured after 72 hours of cooldown. In fact, the surface bandgap was observed to have significantly narrowed relative to the blank NbO ladder structures on all terraces and facets in the 500 × 500 nm scan area that had been monitored for this entire timeline of measurements. The bandgap width on the hydrogen doped surface is approximately 90% of that of the blank ladder structures. This measurement was then repeated by moving around both with the piezo offsets during imaging and by coarse movements across the surface of the crystal with the tip retracted out of tunneling range, and the narrow bandgap was observed in all areas sampled. This result was also reproduced upon repetition of the entire experiment, with the bandgap narrowing after 72 hours of cooldown, and the narrow bandgap being observed in all areas of the surface sampled after 72+ hours cold. Other areas sampled included areas of varying surface defect density, such as facet and step edge density and terrace width, and regardless of defect density the narrow bandgap was measured in all areas of the surface sampled during all repetitions of this experiment. This narrow bandgap is attributed to the presence of hydride phases in proximity to the ladder structures in the sub-surface.

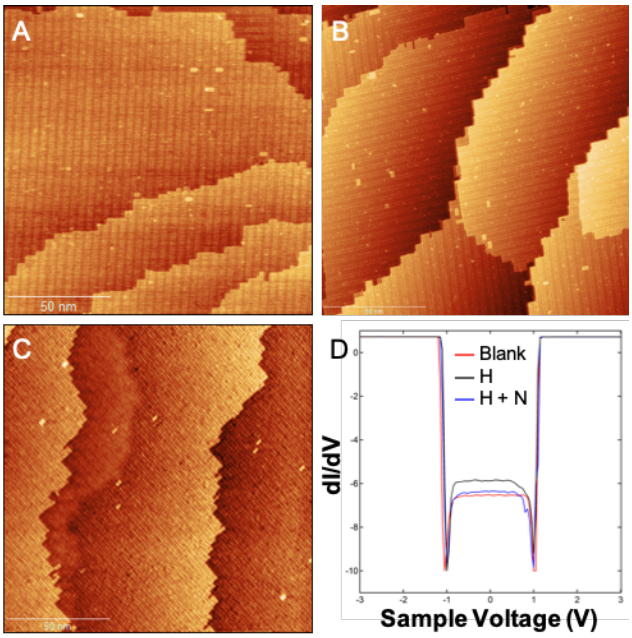

Figure 4.3: STM images taken T_{STM} = 100 K of the Nb(100) (3x1)-O ladder structures following **A:** (blank) no dopant incorporation; **B:** hydrogen doped; **C:** nitrogen and hydrogen doped; **D:** dI/dV spectra for the undoped Nb(100) surface (red), hydrogen-doped sample (black), and hydrogen and nitrogen doped sample (blue) taken within hours of equilibration to T_{STM} = 100 K. Imaging conditions A) 0.72 V, 99 pA; B) 0.55 V, 131 pA; C) 14 mV, 187 pA

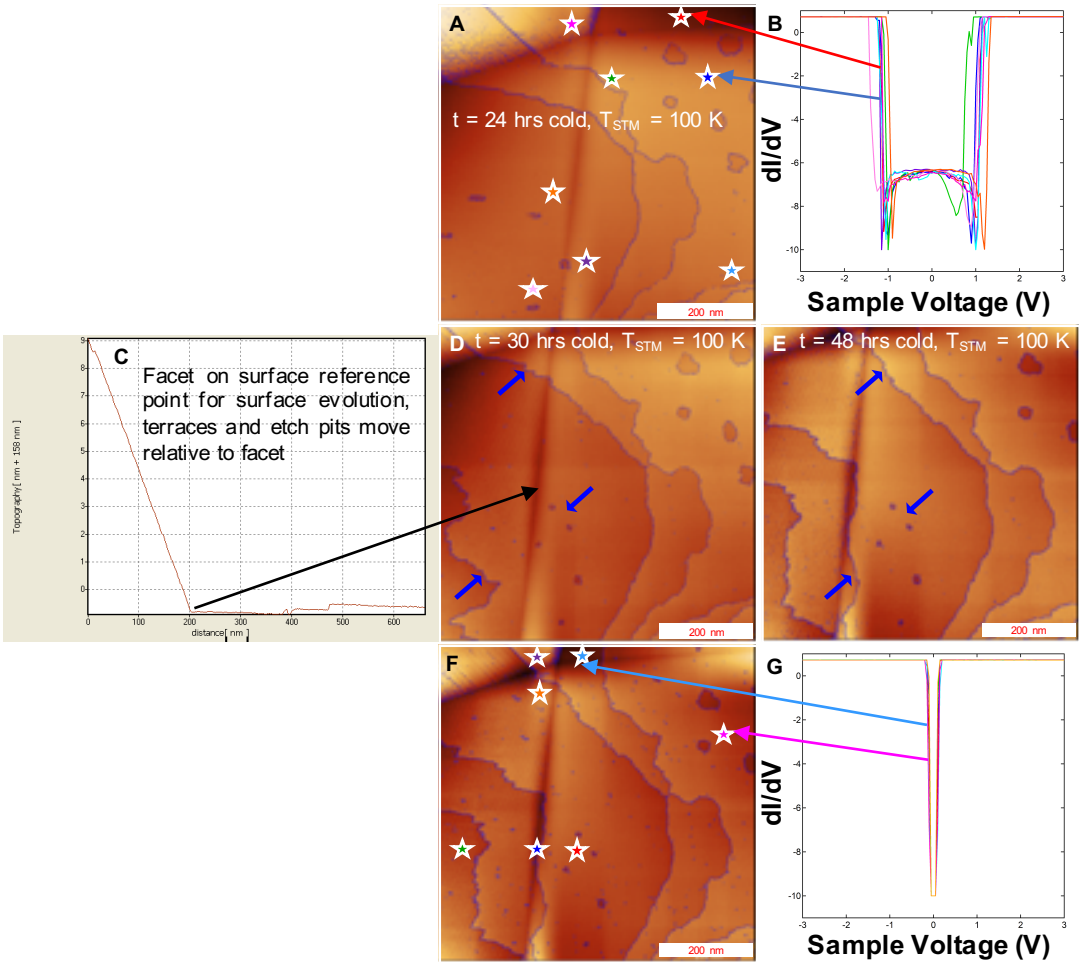

Figure 4.4: A,B: STS locations marked by **stars** showing no change in the surface bandgap relative to the blank ladders on the hydrogen doped surface after 24 hours cold; **C:** topographical linescan showing surface facet (location indicated by **bold arrow)** in STM images used as a positional reference point; **D,E:** surface evolution of hydrogen doped Nb(100) shown *via* 18 hour time-lapse imaging with facet as a positional reference point, relevant step edges and etch pits highlighted in blue with arrows to guide the eye, terraces and etch pits move relative to position of facet; **F,G:** STS locations marked with **stars** show narrowing of surface bandgap relative to blank ladders after 48 hours cold. Imaging conditions A) 0.70 V, 298 pA; C) 101 mV, 300 pA; D) 101 mV, 299 pA; E) 101 mV, 300 pA

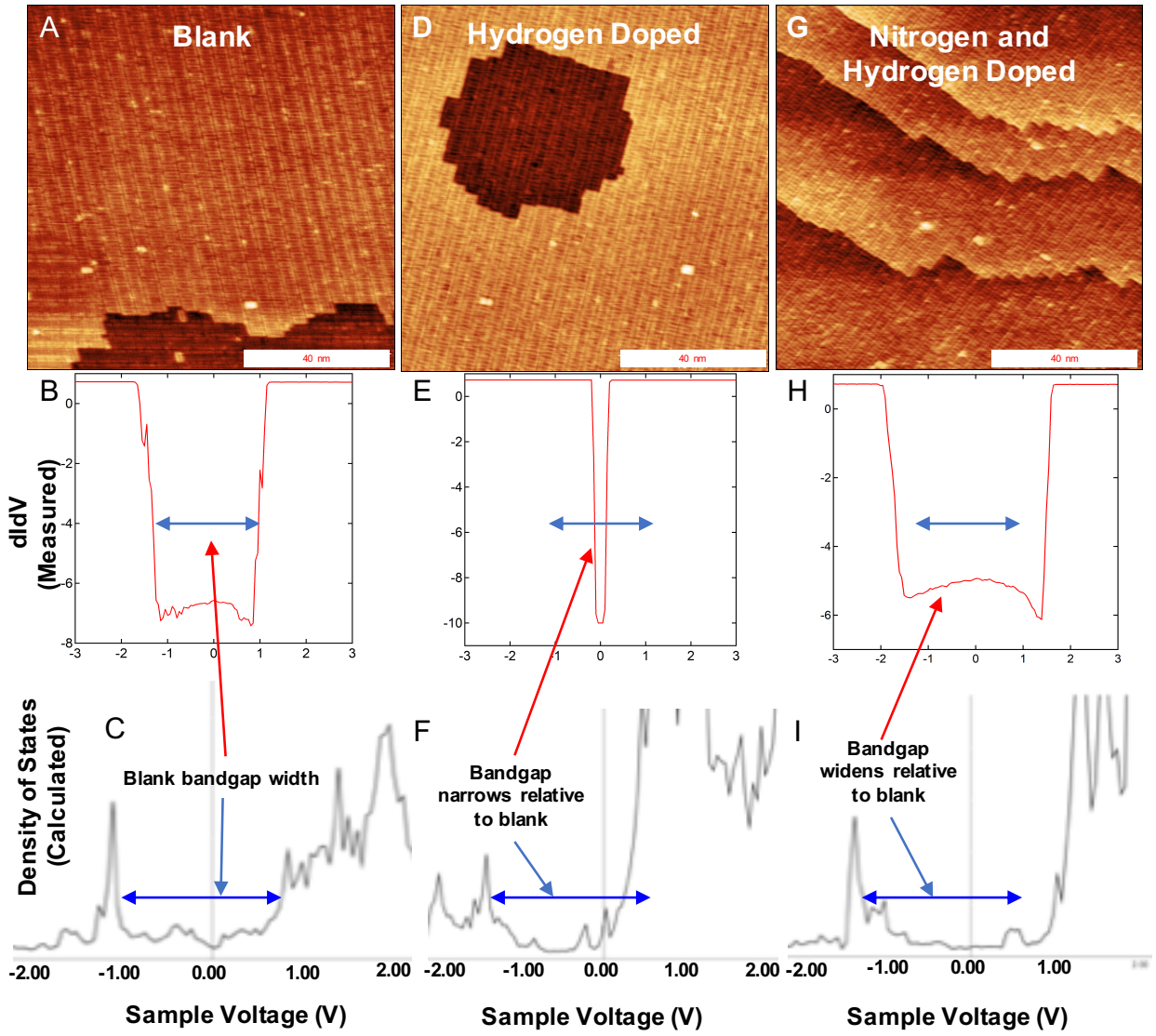

Figure 4.5: STM images taken after ~72 hrs at T_{STM} = 100 K. **A:** Pristine, undoped Nb(100) (3x1)-O surface; **B:** Measured surface bandgap on blank ladders; **C:** DFT calculation of NbO ladder structure surface bandgap, the width of which is shown by the blue arrow; **D:** Hydrogen doped Nb(100) surface; **E:** Measured narrowed surface bandgap indicative of Nb hydride growth; **F:** DFT calculation of Nb hydride sample showing surface bandgap narrowing relative to the pristine NbO surface; **G:** Hydrogen and nitrogen doped Nb(100) surface; **H:** Measured surface bandgap displaying widened gap relative to the undoped ladders; **I:** Calculated surface bandgap of nitrogen infused Nb(100) sample showing a wider surface bandgap relative to the undoped NbO surface bandgap. The raw measured STS data can be seen in **Appendix 2.** Imaging conditions **A:** 0.72 V, 99 pA; **D:** 101 mV, 300 pA; **G:** -0.83 V, 89 pA

This experiment was then repeated for the co-doped surface to determine if the nitrogen doping in any way affected and/or suppressed hydride growth behavior.

A comparison of our STS measurements for all surfaces compared to DFT calculations performed by our theoretical collaborators in the Arias Group is shown in **Figure 4.5**. The undoped NbO ladder structure (STM image in **Figure 4.5a**) surface bandgap was measured as 2 V (**Figure 4.5b**) and supported by DFT calculations showing a ~ 2 V bandgap for the blank ladder structure NbO surface (**Figure 4.5c**). From density functional theory we do not expect the absolute energies to necessarily be exact but the direction of change of the bandgap (narrowing vs. widening) that we observe in our measurements on the hydrogen doped and co-doped surfaces should match with the DFT calculations. An STM image of the hydrogen doped surface is shown in **Figure 4.5d** with the narrow bandgap observed after 72 hours of cooldown in **Figure 4.5e**. The calculated surface bandgap from the Arias group when a hydride β-phase is placed in close proximity underneath the ladder structures in the unit cell construction for the DFT calculation is shown in **Figure 4.5f**. The calculated bandgap narrows relative to the calculated blank, consistent with our measurements, but it only narrows by ~20% even at high concentrations, which is less of a change than what we observe in our measurements. We are still working out with our collaborators on why this may be. Further DFT calculations have shown that placing hydrogen in interstitial sites near the ladders produces occupied states in the middle of the gap, and it may be that the introduction of these states during experimental STS measurements is resulting in a saturation of the current pre-amplifier before we are able to capture the entire gap. The experimental and theoretical results for the co-doped surface are shown in **Figure 4.5g-i**. An STM image of the co-doped surface after 72 hours cold is shown in **Figure 4.5g**. The measured surface bandgap after 72 hours cold is shown in **Figure 4.5h** and compared to the calculated surface bandgap in **Figure 4.5i**. Not only was the

narrow bandgap associated with the hydrogen doped surface not observed after 72 hours of cooldown on the co-doped surface, the surface bandgap was actually observed to significantly widen (**Figure 4.5h**) relative to the blank. The DFT calculations also show a wider bandgap when either a nitride phase or interstitial nitrogen is brought in close proximity to the ladder structures in the unit cell construction. Our combined STS measurements with the calculated bandgaps suggest formation of a nitride phase or nitrogen rich layer in the near surface region interrupting the ability of the Nb hydride phases to precipitate out at the surface. This is consistent with previous first principles calculations that suggest the presence of nitrogen increases the diffusion barrier for hydrogen making it more difficult for niobium hydrides to nucleate.[19] This measurement was extensively repeated all over the co-doped surface in the same manner as on the hydrogen doped surface, and the narrow bandgap associated with the hydrogen doped surface was not observed anywhere. It should be noted that the blank bandgap was still observed in areas after 72+ hours cold, as well as the wider bandgap. This could suggest that even if the nitride/nitrogen rich layer does not cover the entire surface, it is still preventing hydride phases from reaching the surface. The inhomogeneity of the nitride/nitrogen layer across the entire Nb sample could suggest that further optimization of the doping process may result in further gains to Q at operational accelerating gradients.

4.4 Conclusion

Motivated by the profound and reliable benefits to Nb SRF cavity performance of nitrogen doping, we have demonstrated through LT-STM and STS on Nb(100) that nitrogen doping prevents the precipitation of hydride phases at the surface. Phase changes in the near surface cause structural evolution of terraces on the Nb(100) surface, which was observed through overnight

time-lapse STM imaging. Following 72 hrs at T_{STM} = 100 K, the surface bandgap for the hydrogen doped sample was observed to significantly narrow relative to the undoped sample; this narrow bandgap was ubiquitous across the surface for multiple trials. In stark contrast, when doped with both nitrogen and hydrogen, the sample did not exhibit a narrowed bandgap. Rather, the bandgap widened relative to the undoped blank following 72 hrs at T_{STM} = 100 K. Nb hydrides are known to cause hotspot regions of decreased superconductivity on Nb SRF cavities, and lead to power dissipation through the cavity walls. Nitrogen doped cavities do not exhibit these same local hotspots, and our measurements add further experimental evidence to the narrative of nitrogen preventing the hydrides from reaching the surface. Nitrogen doping has a profound effect on cavity performance, increasing Q and reversing the field dependence of Q in the medium field regime, and this study adds to the understanding of the underlying mechanism by demonstrating suppression of hydrides on the nanoscale.

4.5 References

1. Padamsee, H. & Knobloch, J. *RF Superconductivity: Science, Technology and Applications,* 1st Ed.; WILEY-VCH: Weinheim, 2009; p 42.
2. Padamsee, H. The science and technology of superconducting cavities for accelerators. *Superconducting Science Technology,* **2001,** *14,* 28–51.
3. Antoine, C. Materials and surface aspects in the development of SRF Niobium cavities. EuCARD-BOO-2012-001, August 9, 2012.
4. Finnemore, D. K., Stromberg, T. F. & Swenson, C. A. Superconducting Properties of High-Purity Niobium. *Physical Review,* **1966,** *149,* 231-243.

5. Daccà, A., Gemme, G., Mattera, L. & Parodi, R. XPS analysis of the surface composition of niobium for superconducting RF cavities. *Applied Surface Science,* **1998,** *126,* 219-230.
6. Farrell, H. H. & Strongin, M. The interaction of oxygen and nitrogen with the niobium (100) surface: I. Morphology. *Surface Science,* **1973,** *38,* 18-30.
7. Farrell, H. H., Isaacs, H. S. & Strongin, M. The interaction of oxygen and nitrogen with the niobium (100) surface: II. Reaction kinetics. *Surface Science,* **1973,** *38,* 31-52.
8. Grassellino, A. *et al.* Nitrogen and argon doping of niobium for superconducting radio frequency cavities: a pathway to highly efficient accelerating structures. *Superconducting Science Technology,* **2013,** *26,* 102001.
9. Romanenko, A., Grassellino, A., Barkov, F. & Ozelis, J. P. Effect of mild baking on superconducting niobium cavities investigated by sequential nanoremoval. *Physical Review Special Topics. – Accelerators and Beams,* **2013,** *16,* 012001.
10. Trenikhina, Y., Grassellino, A., Melnychuk, O. & Romanenko, A. Characterization of Nitrogen Doping Recipes for the Nb SRF Cavities. MOPB055 (2015). doi:10.18429/JACoW-SRF2015-MOPB055.
11. Dhakal, P., Ciovati, G., Kneisel, P. & Myneni, G. R. Enhancement in Quality Factor of SRF Niobium Cavities by Material Diffusion. *IEEE Transactions on Applied Superconductivity,* **2015,** *25,* 1-4.
12. Barkov, F., Romanenko, A., Trenikhina, Y. & Grassellino, A. Precipitation of hydrides in high purity niobium after different treatments. *Journal of Applied Physics,* **2013,** *114,* 164904.
13. Romanenko, A., Barkov, F., Cooley, L. D. & Grassellino, A. Proximity breakdown of hydrides in superconducting niobium cavities. *Superconducting Science and Technology,* **2013,** *26,* 035003.

14. Barkov, F., Romanenko, A. & Grassellino, A. Direct observation of hydrides formation in cavity-grade niobium. *Physical Review Special Topics – Accelerators and Beams,* **2012,** *15,* 122001.

15. Antoine, C. Z. & Berry, S. H in Niobium: Origin And Method Of Detection. *AIP Conference Proceedings,* **2003,** *671,* 176-189.

16. Knobloch, J. The "Q disease" in Superconducting Niobium RF Cavities. *AIP Conference Proceedings,* **2003,** *671,* 133-150.

17. Bonin, B. & Roth, R. W. *Q degradation of niobium cavities due to hydrogen contamination.* Proceedings of the Fifth Workshop on RF Superconductivity, Hamburg, Germany, October 21, 1991, 210–244.

18. Antoine, C.Z., Aune, B., Bonin, B., Cavedon, J.M., Juillard, M., Godin, A., Henriot, C., Leconte, P., Safa, H., Veyssiere, A., Saclay, C.E., Chevarier, A., Roux, B. *The role of atomic hydrogen in Q-degradation of niobium superconducting rf cavities: analytical point of view.* Proceedings of the Fifth Workshop on RF Superconductivity, Hamburg, Germany, October 21, 1991, 616-634.

19. Garg, P., Balachandran, S., Adlakha, I., Lee, P.J., Bieler, T.R., Solanki, K.N. Revealing the role of nitrogen on hydride nucleation and stability in pure niobium using first principles calculations. *Superconducting Science Technology,* **2018,** *31,* 115007.

20. Gonnella, D. A. The fundamental science of nitrogen-doping of niobium superconducting cavities. Ph.D. Dissertation, Cornell University, Ithaca, NY, 2016.

21. Groll, N.R., Becker, C., Ciovati, G., Grassellino, A., Romanenko, A., Zasadzinski, J.F., Proslier, T. Insight into bulk niobium superconducting RF cavities performances by tunneling spectroscopy. *ArXiv180506359 Cond-Mat Physicshep-Ex*, 2018.

22. Veit, R. D., Kautz, N. A., Farber, R. G. & Sibener, S. J. Oxygen dissolution and surface oxide reconstructions on Nb(100). *Surface Science,* **2019,** *688,* 63-68.

23. Li, Y. *et al.* Surface structure of niobium-dioxide overlayer on niobium(100) identified by scanning tunneling microscopy. *Journal of Applied Physics,* **2001,** *89,* 4772-4776.

24. Yang, Z.Q., Lu, X.Y., Lin, L., Zhao, J.F., Yang, D.Y., Tan, W.W. *TOF-SIMS Study of Nitrogen Doping Niobium Samples.* Proceedings of SRF2015, Whistler, BC, Canada, 2015, 169-173.

25. Grassellino, A., Romanenko, A., Trenikhina, Y., Checchin, M., Martinello, M., Melnychuk, O.S., Chandrasekaran, S., Sergatskov, D.A., Posen, S., Crawford, A.C. Unprecedented quality factors at accelerating gradients up to 45 MVm-1 in niobium superconducting resonators via low temperature nitrogen infusion. *Superconducting Science Technology,* **2017,** *30,* 094004.

26. Ford, D. C., Cooley, L. D. & Seidman, D. N. First-principles calculations of niobium hydride formation in superconducting radio-frequency cavities. *Superconducting Science Technology,* **2013,** *26,* 095002.

27. Ford, D. C., Cooley, L. D. & Seidman, D. N. Suppression of hydride precipitates in niobium superconducting radio-frequency cavities. *Superconducting Science Technology,* **2013,** *26,* 105003.

Chapter 5: Future Directions

The ultimate goal of continuing to improve the performance and reduce the extreme costs of particle accelerator facilities will depend on achieving higher *Q*s, higher accelerating gradients, and higher operating temperatures. This innovation will depend on advances in SRF cavity R&D. Nitrogen doping of niobium cavities has produced revolutionary achievable quality factors. Nitrogen doped Nb SRF cavities reliably achieve quality factors of up to a factor of 3 higher than standard electropolished cavities at the operating temperature of 2 Kelvin and the operational gradient of the state-of-the-art superconducting X-ray free electron laser, the LCLS-II, of 16 MV/m. The theoretical critical field before niobium superconductivity will quench corresponds to an accelerating gradient of ~45 MV/m. There are still unsolved mechanisms of intolerable *Q* degradation at higher gradients. Because of the high *Q*s already achievable with Nb, the most realistic method of reducing the cost of accelerator facilities will be to increase the accelerating gradient to reduce the total length of accelerator needed for modern applications, or to raise the operating temperature to reduce the cost of the cryogenic infrastructure needed to run the accelerator. The latter particularly will depend on the development of new, robust, superconducting materials. The material of choice in the SRF community for the future of superconducting accelerators is Nb_3Sn.

Nb_3Sn is the material of choice for future accelerator applications for a variety of reasons. The material is brittle, which is poor for the complex geometries required of SRF cavities, but Nb_3Sn films can be easily grown on already manufactured pure Nb cavities by tin deposition in a vacuum furnace. Tin chloride is first deposited on the Nb cavity surface to create tin nucleation sites and then tin is evaporated onto the cavity surface to grow a layer of Nb_3Sn on the Nb. The key property of a Nb_3Sn coated cavity which makes it such a promising material is the higher

superconducting critical temperature of Nb_3Sn of 18.3 K, versus 9.2 K of pure Nb. This higher critical temperature allows for a higher SRF cavity operating temperature of 4.2 K. Niobium cavities operate at 2 K, and the jump from 2 K to 4.2 K is of massive importance, because it allows the cavity to operate at the temperature of the surrounding liquid helium bath. It is not the use of the cryogen that is the driver of the cryogenic cost because of the use of liquid helium recyclers, but rather the expensive cryogenic infrastructure needed to cool the cavities below the temperature of liquid helium. Nb_3Sn can solve that entirely by operating at 4.2 K. This could reduce a $30 million dollar cryogenic plant that takes up an entire city block to a $50,000 expense. There is one catch, and that is Nb_3Sn coated cavities do not yet achieve the Q necessary to replace pure Nb.

Nb_3Sn coated cavities currently beat pure Nb in terms of Q at 4.2 K, but Nb_3Sn at 4.2 K does not yet beat Nb at 2 K. This milestone must first be reliably accomplished before Nb_3Sn will be used to construct an accelerator. Much of this will depend on innovations in the growth process of the Nb_3Sn layer. There are still a lot of inconsistencies in the deposition process, such as inhomogeneity in the film thickness across the cavity surface. Local areas with thinner films can exhibit higher surface resistance and therefore degraded Q. A lot of this can be helped by finer control of the underlying Nb grain size, as Sn diffusion happens at the grain boundaries, but if this was the only issue, Nb_3Sn cavities would already be making Nb cavities obsolete. A lot of fundamental research is still needed to understand all of the new Q degradation phenomena that are introduced by the growth process of the Nb_3Sn.

To contribute to the understanding of the growth process of Nb_3Sn on Nb, the Sibener Group is preparing to begin experiments on the initial deposition process of Sn on single crystal Nb(100). We can accomplish this through e-beam evaporation of Sn onto our prepared model surface, the Nb(100) (3x1)-O ladder structures, which was the same model system used for all of

the experiments outlined in this thesis. This will allow us to characterize sub-monolayer Sn deposition on the niobium with the scanning tunneling microscope, and give us insight into preferred adsorption sites of the Sn. We will then be able to study Sn incorporation into the Nb lattice by annealing the Nb crystal after surface Sn adsorption to promote tin incorporation into the surface. By experimenting with the amount of Sn and annealing temperature, we can gain currently unknown insight into the initial atomic-scale nucleation and growth process of the alloy on the metal. This atomic-scale insight into the growth process will provide information that is currently inaccessible to SRF R&D physicists who instead perform ensemble measurements on entire Nb_3Sn coated Nb cavities. Our STM measurements on initial Sn deposition will be able to help inform new and future innovations in the growth procedure.

Chapter 6: Conclusion

Motivated by mild bake treatments of niobium SRF cavities, oxygen dissolution and surface oxide reconstructions were studied with Auger electron spectroscopy (AES) and scanning tunneling microscopy (STM) on the model system the Nb(100) (3x1)-O ladder structures. The model system was chosen because the surface roughness of polycrystalline technical Nb coupons is too extreme to achieve a serviceable level of resolution with the STM. The STM allows for atomic-scale resolution that provides novel insight into SRF relevant surface treatments of Nb cavities. The single crystal Nb(100) surface exhibits atomically-flat terraces and monatomic step edges which are ideal for STM studies after preparation in vacuum, which includes extensive ion-sputtering and annealing to clean the crystal of impurities. As stated earlier, it takes about a month of UHV work to clean one of these Nb(100) crystals. Because of this, all experiments in this thesis were performed on the same crystal. Preparing three Nb(100) crystals and storing them in UHV would be worth the time it would take for a future researcher on this project. This would greatly reduce the time it takes to re-prepare the surface between different types of experiments.

The dissolution of the native oxide layer was studied with AES on the prepared (3x1)-O surface. The oxide layer is ~5 nm thick and consists of the pentoxide at the outermost solid-gas interface, with the dioxide, a series of Nb_xO_y sub-oxides, and the monoxide between the pentoxide and the Nb metal. If the layer is removed, such as when the crystal is cleaned in UHV, the full layer can be grown again by re-exposure to air. For these measurements, the native layer was regrown by simply removing the crystal from vacuum and then immediately pumping it back down. The crystal surface was monitored for oxygen content with AES while the crystal was annealed at 450 K, 500 K, 550 K, and 600 K, to study both the temperature dependent rate and

extent of the dissolution of the oxide layer. An activation energy of 0.6 eV/atom was calculated for this process from the temperature dependent rate constants.

The effect of oxygen dissolution on the ladder structures was studied with the STM. The (3x1)-O surface was prepared after the measurements on the oxygen dissolution were wrapped up. While the crystal was in the STM stage, with the tip retracted out of tunneling range and walked back up the RHK beetle puck ramp, the crystal was exposed to oxygen leaked into the STM chamber *via* the leak valve. The surface was imaged with the STM after exposure and bright spots were observable on the exposed surface Nb atoms of the ladder structures indicative of oxygen chemisorption. The tip was then retracted yet again and the crystal was annealed at 725 K to promote oxygen dissolution through the ladder structures into the bulk. This temperature is below the threshold at which the ladder structures would regrow, which would be undesirable for the experiment. The surface was then again imaged with the STM to characterize the effects of oxygen dissolution. The ladder structures were visibly disrupted, and it was clear that the oxygen dissolution began to break up the ladders making the average length shorter. This process was repeated and the disruption of the ladders continued. A new modal ladder width of 5 Nb atoms was observed, which is exactly half the modal width of the ladders on the pristine surface, suggesting a possible preferential site for oxygen dissolution at the halfway point of the ladder rungs. These STM measurements provided the first atomic-scale visualization of the changing structure of the oxide/metal interface that results from oxygen dissolution.

After the oxygen experiments were wrapped up, the rest of my time here in the Sibener Group was spent working on the hydrogen and nitrogen doped Nb(100) experiments to study nanoscale hydride growth and suppression behavior. This was of course directly motivated by the discovery of the nitrogen doping process for Nb SRF cavities discovered at Fermilab, and was the

hot button topic in the SRF community at the time that I was awarded a graduate research fellowship from Fermilab to study SRF relevant processes. The first milestone that had to be reached was to incorporate relevant amounts of hydrogen into the crystal. The full oxide layer or even the NbO ladder structures will block any hydrogen (or any gas) from entering the Nb metal when present on the surface. In vacuum, the crystal must to be heated to promote the surface oxygen to bury into the sub-surface to incorporate dopants from the ambient into the bulk metal. Niobium will begin to absorb hydrogen under UHV conditions at temperatures above 700 K, and at temperatures above 900 K bulk desorption becomes significant. For this reason, 800 K was chosen as the temperature at which to dope the crystal with hydrogen. The crystal was doped by backfilling the chamber with ultra-high purity hydrogen gas through the leak valve on the prep chamber. The hydrogen was then measured with the residual gas analyzer by desorbing it from the crystal with an e-beam temperature ramp from 800 K to 1200 K. While it is impossible to calculate the absolute amount of desorbed hydrogen, the desorption peak can be integrated to determine if the doping procedure is consistent from trial to trial. The amount of hydrogen was steadily increased until hydride growth behavior was observed with the STM. It is known that the most dangerous temperature region for hydride growth in SRF cavities is between 90 K and 130 K, and 100 K is an easily achievable temperature by simply manipulating the flow of liquid helium in the STM flow cryostat, so 100 K was chosen as the experimental temperature at which to study hydride growth behavior.

During my initial trials of this experiment, I was not entirely sure what the hydride growth behavior would look like under the STM. Large hydrides had been observed with an optical microscope on cavity coupons with very large hydrogen concentrations, enough to cause *Q*-disease in the cavities. I was initially expecting to see nanoscale protrusions that were the beginnings of

hydride precipitates with the STM on the hydrogen doped surface, but this turned out to not be the case. There is one data set that I did not include in this thesis where I observed the growth of an island in the middle of a terrace on an overnight time-lapse STM scan. I never observed this happening again. The two explanations that I have for this is that I simply got very lucky with the location of the STM tip, or that through many repeated trials of this experiment and the formation of hydrides the crystal surface was changed over time and became more defect dense. I believe the latter to be true because while there are certainly always areas of the surface with varying levels of step density and terrace width, I have observed over time a greater occurrence of high step density areas as well as a higher occurrence of sharp facets on the surface, such as the one used as a positional reference in Chapter 4. The structural change that ended up being reproducible on every trial of the experiment was this lateral movement of the surface atoms that is observable when the STM tip is left scanning over the same area for many hours in a row with a positional reference point, such as a facet. The facet is necessary because if the tip is left scanning over a flat area of the surface, this type of movement would be indistinguishable from thermal drift. The lateral surface evolution can be observed over very large time scales by leaving the STM tip scanning overnight in the same area.

The other change that is observed on the hydrogen doped surface is the narrowing of the surface bandgap after 72 hours cold. Once I had discovered this, I performed two full repetitions of this experiment, imaging and measuring the surface bandgap for 5 days cold. During each trial, the bandgap did not narrow until the third day. I performed overnight STM imaging to capture the surface structural evolution, but I did not leave the STS measuring continuously overnight to capture a more precise time of when the narrowing occurred. But, in both trials this would have happened sometime between the second evening of cooldown and the third morning. This

narrowing of the gap is discrete, it does not gradually narrow over time, it goes from the blank gap for the first two days to the narrow gap on the third. Each trial, the crystal was monitored for three days (days 3,4,5) after the narrow bandgap was first observed, to try and locate any area of the surface that did not have the narrow surface bandgap. Every area sampled had the narrow surface bandgap. Zooming in with the microscope, the ladder structures are still present, so the change is caused by a hydride phase in the sub-surface in very close proximity to the ladder structures. This is supported by DFT calculations by our theoretical collaborators who can place hydride phases underneath the ladder structures in their unit cell constructions and calculate the surface bandgap.

When this experiment was repeated on the co-doped surface, the narrow bandgap was not observed despite repeating the measurement for five days of cooldown. In fact, after 72 hours, the bandgap was measured to be significantly wider relative to the blank in areas. This is also supported by DFT calculations when either a nitride phase or interstitial nitrogen is placed in close proximity to the ladder structures. While this wide gap is measured in areas and the blank in others, the narrow bandgap is not observed on the co-doped surface. The measured wide bandgaps with the support of the calculated gaps suggest the existence of a nitride or interstitial nitrogen rich layer in the sub-surface that is preventing the hydrides from reaching the surface. Further work with our collaborators will hopefully tease out further details of the exact nature of the interactions going on between the nitrogen and the hydrogen in the sub-surface. Perhaps the insight we gain will eventually lead to further optimization of the nitrogen doping procedure for niobium SRF cavities.

Appendix 1: Supplementary Figure and Raw Data Referenced for Figure 3.2b

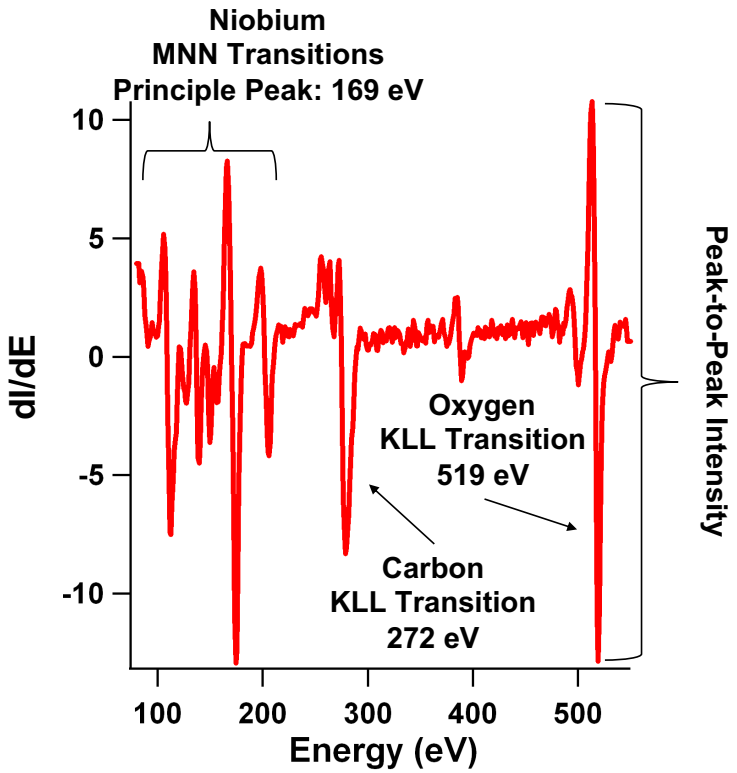

Figure A.1.1: Representative Auger electron spectroscopy (AES) spectrum used to construct **Figure 3.2b**. The current intensity ratio of oxygen to niobium, I_O/I_{Nb}, was monitored during annealing at various temperatures, T_C, to study the rate and extent of dissolution of the native oxide layer. The ratio was calculated by taking the peak-to-peak intensity of the principle transition of each element, Nb and O, multiplying the peak-to-peak intensities by their relative elemental sensitivity factors, and taking the ratio of the corrected intensities. The relative elemental sensitivity factors, S_x, are found by comparison of the signal from each element to a pure silver target. The correction factors for Nb and O were taken from the Handbook of Auger Electron Spectroscopy, 2nd Edition, published by Physical Electronics Industries, 1976. The sensitivity factors when using a 3 keV electron beam for the Nb MNN transitions is 0.27, and the sensitivity factor for the oxygen KLL transition is 0.50. The equation for I_O/I_{Nb} is therefore:

$$\frac{I_O}{I_{Nb}} = \frac{\frac{I_O}{0.50}}{\frac{I_{Nb}}{0.27}}$$

All of the raw AES data used to construct **Figure 3.2b** is in an electronic repository in the Sibener Group. The file names are as follows:

Raw data files for 450 K trial in Figure 3.2b
290615_1_4_A_a.spk
290615_1_4_A_b.spk
290615_1_4_A_c.spk
290615_1_4_A_d.spk
290615_1_4_A_e.spk
290615_1_4_A_f.spk
290615_1_4_A_g.spk
290615_1_4_A_h.spk
290615_1_4_A_i.spk
290615_1_4_A_j.spk
290615_1_4_A_k.spk
290615_1_4_A_l.spk
290615_1_4_A_m.spk
290615_1_4_A_n.spk
290615_1_4_A_o.spk
290615_1_4_A_p.spk
290615_1_4_A_q.spk
290615_1_4_A_r.spk
290615_1_4_A_s.spk
290615_1_4_A_t.spk
290615_1_4_A_u.spk
290615_1_4_A_v.spk
290615_1_4_A_w.spk
290615_1_4_A_x.spk
290615_1_4_A_y.spk
290615_1_4_A_z.spk
290615_1_4_A_za.spk
290615_1_4_A_zb.spk
290615_1_4_A_zc.spk

Raw data files for 500 K trial in Figure 3.2b
030715_1_6_A_a.spk
030715_1_6_A_b.spk
030715_1_6_A_c.spk
030715_1_6_A_d.spk
030715_1_6_A_e.spk
030715_1_6_A_f.spk
030715_1_6_A_g.spk
030715_1_6_A_h.spk
030715_1_6_A_i.spk
030715_1_6_A_j.spk
030715_1_6_A_k.spk

030715_1_6_A_l.spk
030715_1_6_A_m.spk
030715_1_6_A_n.spk
030715_1_6_A_o.spk
030715_1_6_A_p.spk
030715_1_6_A_q.spk
030715_1_6_A_r.spk
030715_1_6_A_s.spk
030715_1_6_A_t.spk
030715_1_6_A_u.spk
030715_1_6_A_v.spk
030715_1_6_A_w.spk
030715_1_6_A_x.spk

Raw data files for 550 K trial in Figure 3.2b
030815_1_8_A_a.spk
030815_1_8_A_b.spk
030815_1_8_A_c.spk
030815_1_8_A_d.spk
030815_1_8_A_e.spk
030815_1_8_A_f.spk
030815_1_8_A_g.spk
030815_1_8_A_h.spk
030815_1_8_A_i.spk
030815_1_8_A_j.spk
030815_1_8_A_k.spk
030815_1_8_A_l.spk
030815_1_8_A_m.spk
030815_1_8_A_n.spk
030815_1_8_A_o.spk
030815_1_8_A_p.spk
030815_1_8_A_q.spk
030815_1_8_A_r.spk

Raw data files for 600 K trial in Figure 3.2b
040815_2_A_a.spk
040815_2_A_b.spk
040815_2_A_c.spk
040815_2_A_d.spk
040815_2_A_e.spk
040815_2_A_f.spk
040815_2_A_g.spk
040815_2_A_h.spk
040815_2_A_i.spk
040815_2_A_j.spk
040815_2_A_k.spk

Appendix 2: Supplementary Figures

The STS data presented in this thesis was obtained by selecting locations within the STM image at which the spectroscopy would be performed. In each location, 10 spectra would be obtained. This section contains representative sets of 10 spectra from each of the undoped, hydrogen doped, and nitrogen and hydrogen doped surfaces. All of the STS data obtained from the doped Nb(100) experiments is in an electronic repository in the Sibener Group.

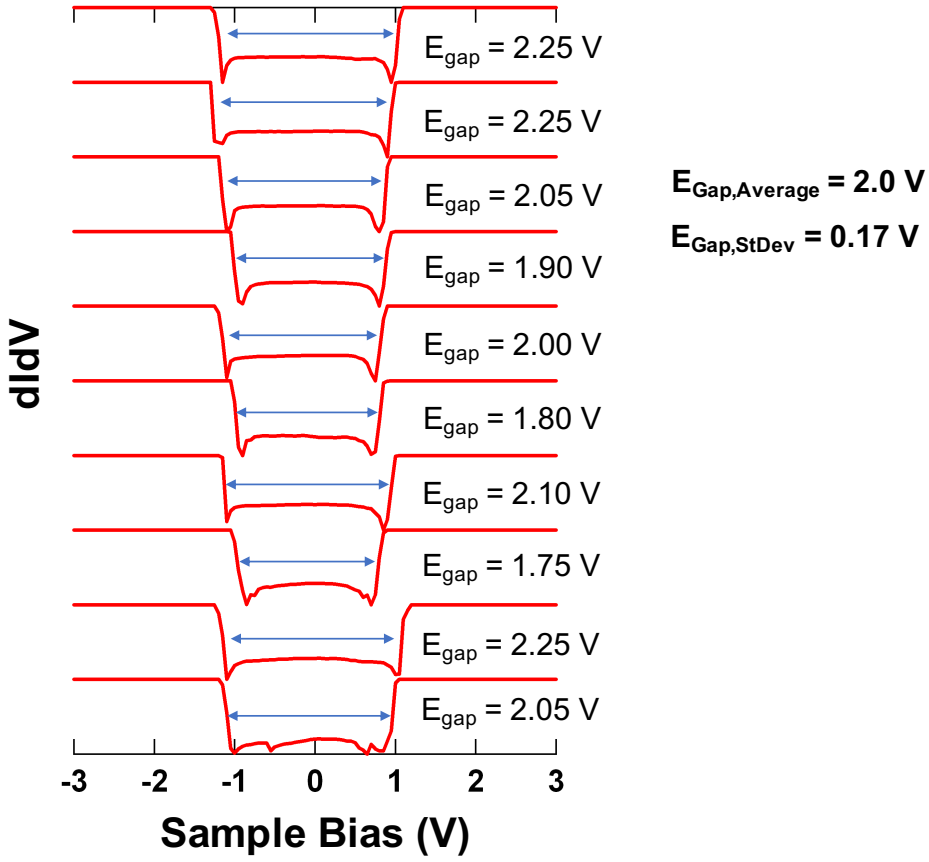

Figure A.2.1: Representative set of 10 curves obtained on the blank (undoped) Nb(100) (3x1)-O ladder structures at T_{STM} = 100 K. All STS data was obtained by selecting locations within the scan area during the STM imaging to perform the spectroscopy. At each location selected, 10 dIdV curves were measured. The measured blank gap that we used for comparison to the doped surfaces is $E_{gap,average}$ = 2.0 V. When there was a fluctuation in the measured bandgap width greater than 3 standard deviations from the average measured value, the measurement was discarded from the statistical analysis of the bandgap widths.

All of the STS data obtained on the blank Nb(100) (3x1)-O ladder structures is saved in an electronic repository in the Sibener Group. The file name for the above dIdV curves shown in **Figure A.1** is listed below:

12182018_blankprep_12202018_100K_12202018005_point5_didv

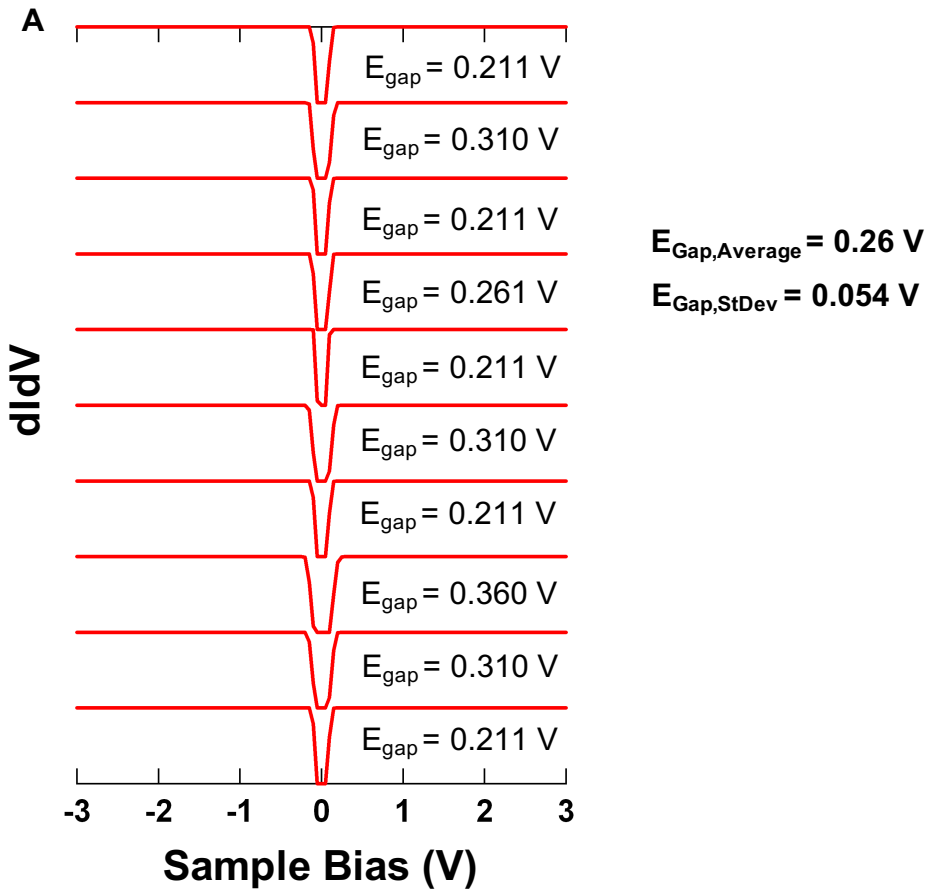

Figure A.2.2: Representative set of 10 dIdV curves obtained *via* STS on the hydrogen doped Nb(100) surface after the STM stage had been held at 100 K for 72 hours. All STS data was obtained by selecting locations within the scan area during the STM imaging to perform the spectroscopy. At each location selected, 10 dIdV curves were measured. The gap in the dIdV after 72 hours of cooldown on the hydrogen doped surface is significantly narrowed ($E_{gap,average}$ = 0.26 V) in comparison to the blank ($E_{gap,avg}$ = 2.0 V) This narrowing did not happen gradually, but rather a discrete shift measured after 72 hours in each trial of the experiment. This narrow bandgap is presumably the result of hydride growth behavior beneath the ladder structures. We are currently working with our theoretical collaborators on getting experiment to match with theory for the dIdV. This will be used to help explain the sub-surface hydride growth behavior that is causing the observed changes in the dIdV.

All of the STS data obtained on the hydrogen doped Nb(100) surface is saved in an electronic repository in the Sibener Group. The file name for the above dIdV curves shown in **Figure A.2** is listed below:

05162019_h2prep_05262019_100K_051620190046_point2_didv

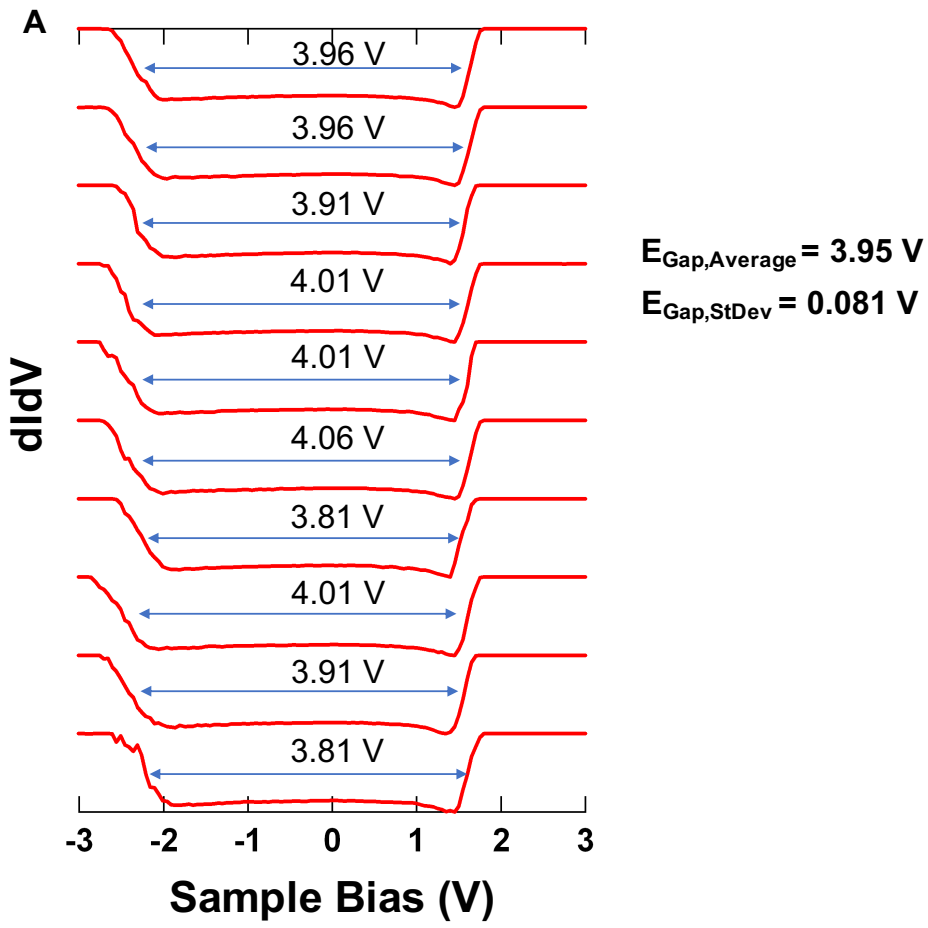

Figure A.2.3: Representative set of 10 dIdV curves obtained *via* STS on the co-doped (nitrogen and hydrogen) Nb(100) surface after the STM stage had been held at 100 K for 72 hours. All STS data was obtained by selecting locations within the scan area during the STM imaging to perform the spectroscopy. At each location selected, 10 dIdV curves were measured. Not only is the narrow bandgap ($E_{gap,average}$ = 0.261 V) of the hydrogen doped surface not observed, but the gap in the dIdV after 72 hours of cooldown on the co-doped surface is significantly wider ($E_{Gap,Average}$ = 3.95 V) in comparison to the blank ($E_{gap,avg}$ = 2.0 V) From preliminary work with our theoretical collaborators, this wide bandgap is the result of a nitride phase or interstitial nitrogen-rich layer beneath the ladder structures that is preventing the hydrides from reaching the surface.

All of the STS data obtained on the co-doped Nb(100) surface is saved in an electronic repository in the Sibener Group. The file name for the above dIdV curves shown in **Figure A.3** is listed below:

06052019_n2h2prep_06092019_100K_060920190022_point24_didv